SKB

TECHNICAL REPORT 90-21

Testing models of redox front migration and geochemistry at the Osamu Utsumi mine and Morro do Ferro analogue study sites, Poços de Caldas, Brazil

J E Cross[1], A Haworth[1], P C Lichtner[2], A B MacKenzie[3], L Moreno[4], I Neretnieks[4], D K Nordstrom[5], D Read[6], L Romero[4], R D Scott[3], S M Sharland[1], C J Tweed[2]

[1] Chemistry Division, Harwell Laboratory, UKAEA, Harwell, UK
[2] Mineralogisch-Petrographisches Institut, Universität, Bern, Bern, Switzerland
[3] Scottish Universities Research and Reactor Centre, Glasgow, UK
[4] Department of Chemical Engineering, Royal Institute of Technology, Stockholm, Sweden
[5] U.S. Geological Survey, Menlo Park, CA, USA
[6] Atkins ES, Epsom, Surrey, UK

Compiled and Edited by: I G McKinley, NAGRA, Baden (Switzerland)

January 1991

SVENSK KÄRNBRÄNSLEHANTERING AB
SWEDISH NUCLEAR FUEL AND WASTE MANAGEMENT CO

BOX 5864 S-102 48 STOCKHOLM

TEL 08-665 28 00 TELEX 13108 SKB S
TELEFAX 08-661 57 19

NAGRA NTB 90-30
SKB TR 90-21
UK DOE WR 90-052

Poços de Caldas Report No. 12

Testing models of redox front migration and geochemistry at the Osamu Utsumi mine and Morro do Ferro analogue study sites, Poços de Caldas, Brazil.

JANUARY 1991

An international project with the participation of Brazil, Sweden (SKB), Switzerland (NAGRA), United Kingdom (UK DOE) and USA (US DOE). The project is managed by SKB, Swedish Nuclear Fuel and Waste Management Co.

TESTING MODELS OF REDOX FRONT MIGRATION AND GEOCHEMISTRY AT THE OSAMU UTSUMI MINE AND MORRO DO FERRO ANALOGUE STUDY SITES, POÇOS DE CALDAS, BRAZIL

J E Cross[1], A Haworth[1], P C Lichtner[2], A B MacKenzie[3], L Moreno[4], I Neretnieks[4], D K Nordstrom[5], D Read[6], L Romero[4], R D Scott[3], S M Sharland[1], C J Tweed[1]

1 Chemistry Division, Harwell Laboratory, UKAEA, Harwell, U.K.
2 Mineralogisch-Petrographisches Institut, Universität Bern, Bern, Switzerland
3 Scottish Universities Research and Reactor Centre, Glasgow, U.K.
4 Department of Chemical Engineering, Royal Institute of Technology, Stockholm, Sweden
5 U.S.Geological Survey, Menlo Park, CA, USA
6 Atkins ES, Epsom, Surrey, U.K.

Compiled and Edited by: I.G. McKinley, NAGRA, Baden (Switzerland).

January 1991

Testing models of redox front migration and geochemistry at the Osamu Utsumi mine and Morro do Ferro analogue study sites, Poços de Caldas, Brazil.

J.E. CROSS[1], A. HAWORTH[1], P.C. LICHTNER[2], A.B. MACKENZIE[3], L. MORENO[4], I. NERETNIEKS[4], D.K. NORDSTROM[5], D. READ[6], L. ROMERO[4], R.D. SCOTT[3], S.M. SHARLAND[1], and C.J. TWEED[1].

[1]Chemistry Division, Harwell Laboratory, UKAEA, Harwell, OX11 ORA (U.K.).

[2]Mineralogisch-Petrographisches Institut, Universität Bern, Baltzerstrasse 1, CH-3012 Bern (Switzerland).

[3]Scottish Universities Research and Reactor Centre, East Kilbride, Glasgow G75 OQU (U.K.).

[4]Department of Chemical Engineering, Royal Institute of Technology, S-100 44 Stockholm (Sweden).

[5]U.S.Geological Survey, Menlo Park, CA 94025 (USA).

[6]Atkins ES, Woodcote Grove, Ashley Road, Epsom, Surrey, KT22 7NE (U.K.).

Compiled and Edited by: I.G. McKinley, NAGRA, Parkstrasse 23, CH-5401 Baden (Switzerland).

Abstract

Redox fronts occur at a number of locations in repository systems and models have been established to describe their chemical evolution and spatial development. Such models can be tested against detailed observations of the well-developed redox fronts at the Osamu Utsumi mine.

Simple scoping calculations can explain the formation of redox fronts in very general terms but greatly simplify the processes known to be occurring at such fronts. Coupled transport / chemistry models can provide a better simulation of the fronts, but these are primarily interpretative models which have not yet displayed any convincing predictive abilities. They tend to be rather poor, in particular, in simulating trace element chemistry in either solution or solid phases.

Interpretative modelling of microbial activity, natural series profiles and trace element distributions gives strong indications of the reasons for the limitations of the chemical modelling. The role of microbial catalysis seems to be very significant in such systems, particularly affecting the redox chemistry of sulphur. Natural series measurements indicate very slow redox front movement at particular sites which could be due to

precipitation processes limiting accessible porosity, a point not considered in any of the models. Finally, the trace element distributions strongly suggest immobilisation of many elements as co-precipitates or solid solutions in secondary iron minerals, again a process not considered by current models.

Zusammenfassung

Redoxfronten entstehen an einer Anzahl von Stellen im Endlagersystem. Zur Beschreibung ihrer chemischen und örtlichen Entwicklung wurden Modelle erstellt. Solche Modelle können anhand von detaillierten Beobachtungen an gut entwickelten Redoxfronten der Osamu Utsumi Mine überprüft werden.

Einfache Ueberschlagsberechungen können die Bildung von Redoxfronten grundsätzlich erklären, aber sie vereinfachen die Prozesse, die offenkundig an solchen Fronten von statten gehen, allzu sehr. Kombinierte Transport/Chemie-Modelle können eine bessere Simulation der Fronten bieten. Es handelt sich dabei jedoch in erster Linie um interpretative Modelle, deren Vorhersagefähigkeit noch nicht bewiesen ist. Sie sind meist ungenügend, vor allem für die Simulation der Chemie von Spurenelementen in Lösung und in festen Phasen.

Interpretationsmodelle von mikrobiologischen Vorgängen, von Profilen der natürlichen Zerfalls-Serien und von Spurenelementenverteilungen deuten auf die Gründe für die Begrenzung chemischer Modelle. Die Rolle der mikrobiologischen Katalyse scheint von sehr grosser Bedeutung für solche Systeme zu sein, vor allem betreffend der Redoxchemie des Schwefels. Messungen natürlicher Zerfalls-Serien deuten an bestimmten Orten auf sehr langsame Rodoxfront-Bewegungen. Dies könnte aufgrund von Fällungsvorgängen, welche die Porosität einschränken, zustande kommen; ein Punkt, der in keinem der Modelle berücksichtigt wurde. Schlussendlich deutet die Verteilung der Spurenelemente stark auf die Immobilisation vieler Elemente durch Mitfällung oder Bildung fester Lösungen in sekundären Eisenmineralien hin; auch ein Vorgang der von gängigen Modellen nicht berücksichtigt wird.

Résumé

Des fronts redox peuvent se présenter en de nombreux endroits dans les systèmes de dépôt en milieu rocheux, et des modèles ont été développés pour décrire leur évolution chimique et spatiale. On peut contrôler de tels modèles au moyen des observations détaillées faites sur les fronts redox bien développés à la mine d'uranium d'Osamu Utsumi.

Des calculs simples peuvent expliquer en termes très généraux la formation de fronts redox, mais ils simplifient à outrance les processus se déroulant sur de tels fronts. Des modèles couplés transport/chimisme peuvent fournir une simulation meilleure des fronts, mais il s'agit en premier lieu de modèles interprétatifs qui n'ont pas encore atteint une capacité prédictionelle convaincante. En particulier, ils se montrent plutôt inaptes à simuler le chimisme des éléments trace, que ce soit en phase solide ou dissoute.

La modélisation interprétative de l'activité microbienne, des profils de séries naturelles et de distribution des éléments trace fournissent de fortes indications des limitations de la modélisation chimique. Il semble que la catalyse microbienne joue un rôle très significatif dans les systèmes redox, agissant particulièrement sur la chimie redox des sulfures. Les mesures de séries naturelles indiquent que le mouvement des fronts redox est très lent à certains endroits. Ceci pourrait être dû à des processus de précipitation limitant l'accès à la porosité ouverte. Cet aspect n'a été pris en compte dans aucun des modèles. Les distributions des éléments trace, enfin, suggèrent fortement que de nombreux éléments sont immobilisés sous forme de co-précipitats ou de solutions solides dans les minéraux secondaires du fer. Ce processus n'a pas non plus été pris en compte dans les modèles utilisés.

Preface

The Poços de Caldas Project was designed to study processes occurring in a natural environment which contains many features of relevance for the safety assessment of radioactive waste disposal. The study area, in the State of Minas Gerais, Brazil, is a region of high natural radioactivity associated with volcanic rocks, geothermal springs and uranium ore deposits. It contains two sites of particular interest on which the project work was focussed: the Osamu Utsumi uranium mine and the Morro do Ferro thorium/rare-earth ore body. The first site is notable in particular for the prominent redox fronts contained in the rock, while Morro do Ferro was already well-known as one of the most naturally radioactive locations on the surface of the Earth, owing to the high thorium ore grade and the shallow, localised nature of the deposit.

The features displayed by these two sites presented the opportunity to study a number of issues of concern in repository performance assessment. The four objectives set after the first-year feasibility study were:

1. Testing of equilibrium thermodynamic codes and their associated databases used to evaluate rock/water interactions and solubility/speciation of elements.
2. Determining interactions of natural groundwater colloids with radionuclides and mineral surfaces, with emphasis on their role in radionuclide transport processes.
3. Producing a model of the evolution and movement of redox fronts, with the additional aim of understanding long-term, large-scale movements of trace elements and rare-earths over the front (including, if possible, natural Pu and Tc).
4. Modelling migration of rare-earths (REE) and U-Th series radionuclides during hydrothermal activity similar to that anticipated in the very near-field of some spent-fuel repositories.

The project ran for three and a half years from June 1986 until December 1989 under the joint sponsorship of SKB (Sweden), NAGRA (Switzerland), the Department of the Environment (UK) and the Department of Energy (USA), with considerable support from a number of organisations in Brazil, notably Nuclebrás (now Urânio do Brasil). The first-year feasibility study was followed by two and a half years of data collection and interpretation, focussed on the four objectives above.

This report is one of a series of 15, summarising the technical aspects of the work and presenting the background data. A complete list of reports is given below. Those in series A present data and interpretations of the sites, while those in series B present the results of modelling the data with performance assessment objectives in mind. The main findings of the project are presented in a separate summary (no. 15).

This report presents a compilation of data which have been modelled to predict the reactions occurring at redox fronts and the rate at which they move. These models have been tested against observations of the well-defined redox fronts at the Osamu Utsumi mine site (objective 3).

Poços de Caldas Project Report Series

Series A: Data, Descriptive, Interpretation

Report No.	Topic	Authors (Lead in Capitals)
1.	The regional geology, mineralogy and geochemistry of the Poços de Caldas alkaline caldera complex, Minas Gerais, Brazil.	SCHORSCHER, Shea.
2.	Mineralogy, petrology and geochemistry of the Poços de Caldas analogue study sites, Minas Gerais, Brazil. I: Osamu Utsumi uranium mine.	WABER, Schorscher, Peters.
3.	Mineralogy, petrology and geochemistry of the Poços de Caldas analogue study sites, Minas Gerais, Brazil. II: Morro do Ferro.	WABER.
4.	Isotopic geochemical characterization of selected nepheline syenites and phonolites from the Poços de Caldas alkaline complex, Minas Gerais, Brazil.	SHEA.
5.	Geomorphological and hydrogeological features of the Poços de Caldas caldera and the Osamu Utsumi mine and Morro do Ferro analogue study sites, Brazil.	HOLMES, Pitty, Noy.
6.	Chemical and isotopic composition of groundwaters and their seasonal variability at the Osamu Utsumi and Morro do Ferro analogue study sites, Poços de Caldas, Brazil.	NORDSTROM, Smellie, Wolf.
7.	Natural radionuclide and stable element studies of rock samples from the Osamu Utsumi mine and Morro do Ferro analogue study sites, Poços de Caldas, Brazil.	MacKENZIE, Scott, Linsalata, Miekeley, Osmond, Curtis.
8.	Natural series radionuclide and rare-earth element geochemistry of waters from the Osamu Utsumi mine and Morro do Ferro analogue study sites, Poços de Caldas, Brazil.	MIEKELEY, Coutinho de Jesus, Porto da Silveira, Linsalata, Morse, Osmond.

Content

1. Introduction

In most concepts for deep disposal of radioactive waste, the environment around the repository will, in its undisturbed form, be chemically reducing. Construction and operation of the repository will inevitably introduce air and hence a boundary between oxidising and reducing zones (a "redox front") will become established. In cases where the host-rock contains sulphide minerals, in particular, the redox front formation and movement may be associated with significant alteration of rock properties and the production of acidic leachates, which could cause further damage to repository structures (McKinley and Bradbury, 1989).

For high-level radioactive waste, in particular spent fuel, further oxidants may be produced after repository closure due to radiolysis (KBS, 1983). Over long periods of time ($\approx 10^7$ years), when flow occurs in distinct fissures, the redox front resulting from this source could potentially penetrate large distances into the host-rock (Neretnieks, 1984).

A number of simple models have been developed to predict the reactions occurring at such redox fronts and the rate at which they move. It is intended to test such models against observations of the well-defined redox fronts at the Osamu Utsumi mine site.

The main aims of this report are:

i) To synthesise evidence to define the form and migration timescales of various redox fronts.

ii) To combine such data with mineralogical data in order to provide input for coupled models of solute transport and chemical reaction.

iii) To compare model predictions with further observational evidence.

This research area involves input from many others and, over the duration of the project, has evolved considerably. The background information used to develop the models is summarised in Chapter 2.

Initial estimates of redox front movement and predominant reactions in this zone were based on simple mass balance calculations as reported in Chapter 3. This first model was subsequently extended to examine the topography of the redox fronts by considering preferential flow paths. Early observations of the geochemistry of the redox front were also used for scoping coupled chemical reaction/solute transport calculations. These suffered from a number of problems, e.g. predicting much more acid groundwater than was actually observed, and were improved to include buffering reactions, to better

represent the inherent heterogeneity of the redox front and to take into account the geomorphological evidence of redox front movement rates. These models are described in Chapter 4.

An alternative modelling approach concentrated on the detailed simulation of geochemical profiles over the front. A major problem with initial versions of this model was again underprediction of pH and inability to simulate the formation of secondary pyrite. In order to improve this model, the local equilibrium condition was abandoned and a kinetic approach adopted. This gave a rather good description of the zones through the redox front, and is described in Chapter 5.

Finally, the chemical modelling results are put in context by considering other evidence from trace element and natural series distributions around the redox front and microbiological studies in Chapter 6. The conclusions drawn are summarised in Chapter 7.

The modelling work in Chapters 3–5 consists of quite distinct studies which are attributed to the individuals involved. All other chapters have been drafted by the editor, following open discussions at modelling workshops and incorporating comments from the co-authors of this report.

2. Description of the redox front and development of conceptual models

The background needed to develop the models described herein is discussed in detail in other reports in this series. This chapter gives a brief overview of the information available (giving source references) and indicates how the conceptual models involved were derived from this database.

2.1. Geology, mineralogy and topography

The sharp redox fronts are one of the most characteristic features of the Osamu Utsumi mine, the overlying (oxidising) rock being brownish-red due to iron oxyhydroxides while the underlying reduced rock is grey in colour and contains disseminated pyrite. The present redox boundary forms fingers or wedges where oxidised rock penetrates reduced zones, generally associated with fractures or shear zones (Fig. 1). Fractures penetrating the reduced zone may also show evidence of oxidising channels.

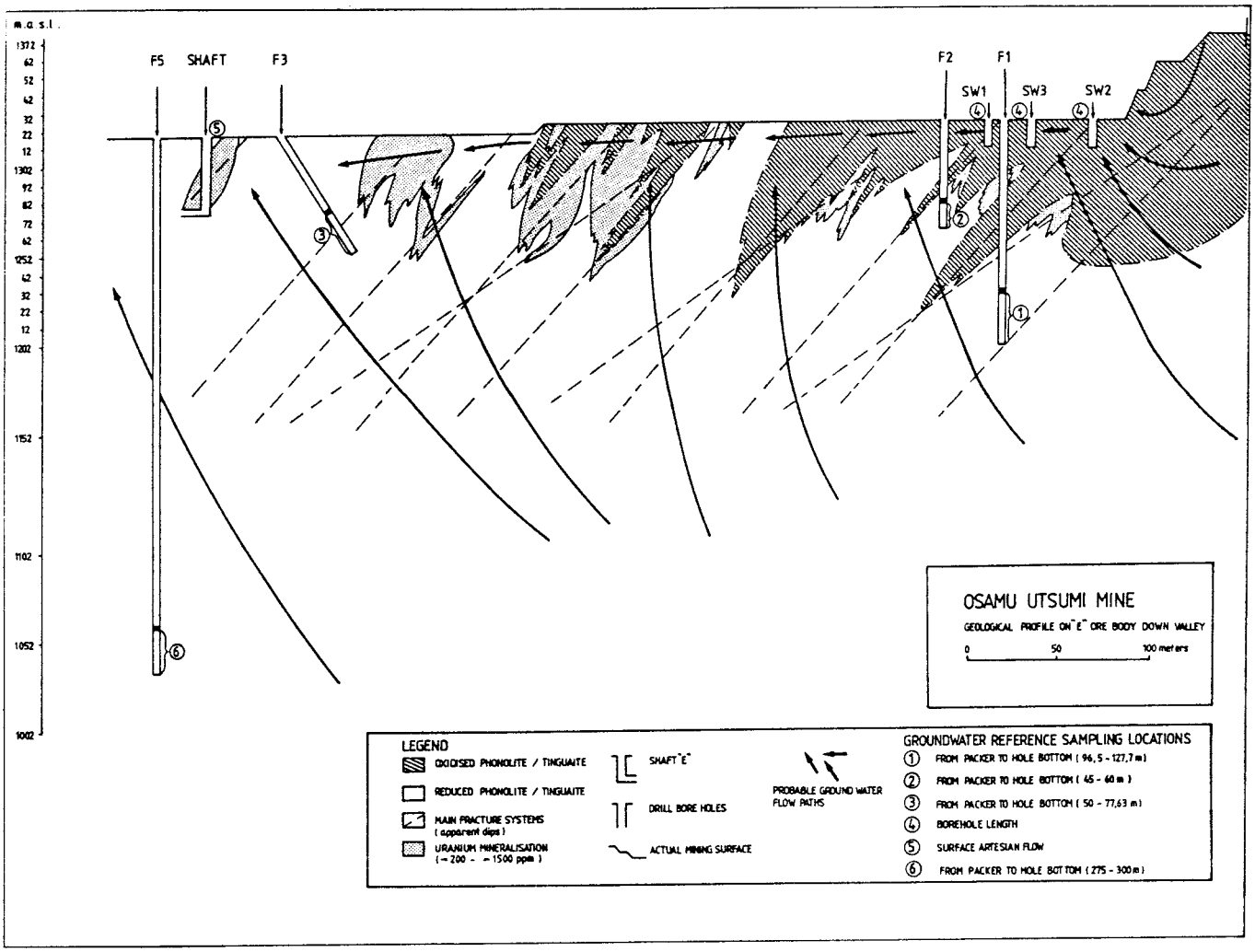

Figure 1. Cross-section of the Osamu Utsumi mine showing borehole locations, redox fronts, mineralised zones, groundwater reference sampling points and the general direction of groundwater flow.

The origin of the uranium ore body at the Osamu Utsumi mine and its associated mineralogy is described in detail by Waber *et al.* (this report series; Rep. 2). From the detailed mineralogy it is clear that solute transport occurs over the redox front. On the reduced side of the front secondary pyrite forms, which is morphologically and isotopically distinct from the original primary pyrite. In particular areas, uranium mineralisation, in the form of pitchblende nodules, is also found on the reducing side of the front. Locally, a clay-rich (kaolinite) layer may be observed at the redox front. In addition to the redox front, a less obvious hydrolytic front can be identified which defines the limit of rock alteration by near-surface fluids (weathering).

Remnant traces of surface-oxidised pyrite and pitchblende nodules give indications of movement of the front. Geomorphological studies (Holmes *et al.*, this report series; Rep. 5) give an estimate of the average erosion rate in this area of ≈ 12 m/Ma which, although local variations are to be expected, gives an estimate of a steady state rate of movement of the front. Hydrogeological modelling (Holmes *et al.*, op. cit.) indicates that, before excavation of the mine, the predominant advective flux, along the flanks of the valley, was in a downward direction. Even though measured hydraulic contrasts in test boreholes are rather small, the aspect ratio ($\approx 4:1$) of oxidising fingers argues for advective flow focussed along fissure zones.

2.2. Geochemistry

Hydrogeological modelling (Holmes *et al.*, op. cit.) indicates that the current flow system has been perturbed by the presence of the mine. This is partially supported by hydrochemical analyses (Nordstrom *et al.*, this report series; Reps. 6 and 14) which indicate fairly active circulation down to ≈ 50 m. Three water zones are observed:

a) above ≈ 10 m are acidic waters with high concentrations of Fe, U, F and SO_4,

b) in the range ≈ 10 m – 50 m below surface, the waters show decreased Fe, U, F and SO_4, along with increased pH and alkalinity and moderately oxidising conditions,

c) below 50 m, nearly all Fe is present as Fe(II) and U concentrations are low, implying reducing conditions.

Whole-rock analyses show considerable concentrations of many trace elements around the redox front (MacKenzie *et al.*, this report series; Rep. 7). Elements are concentrated on either one or both sides of the fronts and some general trends in elemental chemistry can be observed. Symmetrical profiles over the front for particular trace elements suggest that solute transport over the front may occur predominantly by diffusion or that any advective transport occurs in the plane of the front at these locations.

Natural series measurements (MacKenzie *et al.*, op. cit.) indicate that the rate of movement of the redox fronts is slow (~m/Ma scale) and may vary significantly between different locations.

Microbiological analysis and modelling (West *et al.*, this report series; Rep. 10) indicate significant biological activity at the front, which is supported by the secondary pyrite S-isotope data (Waber *et al.*, op. cit.)

2.3. Development of conceptual redox front models

The very simplest model of the redox front considers only the input of a given flux of oxidising (air-saturated) rainwater at the surface which then advects downwards with subsequent oxidation of pyrite. By a mass balance calculation, the rate of movement of the front can be derived. The observed marked fingering of the front can be taken into account by assuming that advection occurs only within fractures and is focussed in channels within the plane of these fractures. Transport of solute from the advective flow zones into the surrounding rock is assumed to occur by diffusion. This model was the first to be quantitatively analysed and is described in Chapter 3.

The observed geochemistry clearly necessitates a more rigorous analysis of the reactions occurring at the front. For the case described, the large-scale flow system is not considered in detail and only the evolution of the mineralogy and pore-water chemistry in a small section of the redox front is considered. In Chapter 4.1, such a coupled model is analysed quantitatively for cases in which solute transport occurs by advection or diffusion. Apart from pyrite oxidation, this model also considers the alteration of K-feldspar to form kaolinite and chalcedony, and uraninite formation.

A second geochemical model, described in Chapter 4.2, considers the general distribution of uranium in more detail. Two zones are identified, an upper (oxidised) region in which uranium retention is modelled by a sorption mechanism, and the redox

front itself. The front, and the solute transport across it, were assumed to occur by diffusion and by precipitation of various uranium minerals.

Both of these geochemical models assume thermodynamic equilibrium to be rapidly achieved. A third model, which explicitly includes consideration of the kinetics involved, is presented in Chapter 5. This model considers how the chemistry of a package of water changes as it is advectively transported through the rock body. This approach considers both oxidation and mineral alteration reactions.

3. Mass balance calculations and simulation of redox front topography

I. Neretnieks, L. Moreno, and L. Romero

The aim of this study was to examine the extent to which rather simple models of redox front processes were compatible with field observations. In the simplest model, the rate of movement of the redox front is estimated from the supply of oxidants. The model makes the global assumptions of:

i) A rainfall infiltration excess of 100 mm/year.

ii) Oxygen saturation in percolating water (10 ppm).

iii) Two percent pyrite by weight in the reduced rock.

iv) Complete pyrite oxidation by dissolved oxygen, i.e.
$Fe S_{2(s)} + 15/4\ O_{2(aq)} + 7/2\ H_2O \rightarrow Fe(OH)_{3(s)} + 4H^+ + 2SO_4^{2-}$.

v) No other redox active components in the system.

This results in a predicted redox front movement rate of $\approx$25 m/10^6 years. Further calculations have also examined the effects of molecular diffusion. In the simplest case zero advection is assumed, which would correspond to a location in which the water was completely stagnant. In this instance the rate of movement of the front would be <1 m/Ma. Calculations have also examined the consequences of including diffusion in the advective model but, as expected, the net effect on the rate of the front movement is minor.

This first set of calculations assumes an ideal homogeneous, porous, anisotropic rock. In reality, the redox front shows marked fingering (Fig. 1) which has been mapped in

some detail. Within the area of the mine ($\approx$600x360 m), some 200 individual fingers were mapped.

In order to analyse these redox fingers, a conceptual model was developed in which advective flow occurs only within fracture zones; these fracture zones are themselves heterogeneous and contain channels in which the flow is focussed. Oxidants in the flowing water may, however, diffuse into the surrounding rock, which is assumed to have a continuous connected porosity.

The rock is assumed to contain a large number of channels which may have different flow-rates and widths. Figure 2 shows a cross-section of rock with independent channels. Every channel has, on average, a cross-section of rock which may be oxidised by oxygen diffusing from that channel. The channels are independent for some distance, but otherwise are part of a channel network.

The mathematical model was based on the assumption of fast reaction and a cylindrical geometry for the spreading of the redox front from the channel. The solution to the advective transport and diffusion equations was developed using the same method as Cooper and Liberman (1970). For a constant flow-rate, a semianalytical solution was obtained. When erosion was included and the water flow-rate was allowed to vary with time, a numerical scheme based on implicit techniques was used.

There is no information on widths, frequency and flow-rate distribution of channels in the rock in the uranium mine. There are, however, observations from several tunnels in crystalline rocks in Sweden which show that channel widths range from a few centimetres to tens of centimetres and up to a metre. The frequency of channels ranges from 1 per 20 m^2 in Stripa (Abelin *et al.*, 1985) to about 1 per 100 m^2 in SFR (Bolvede and Christianson, 1987) and Kymmen (Palmqvist and Stanfors, 1987) in competent rock. In fracture zones in Kymmen the frequency was nearly an order of magnitude larger. The flow-rates vary considerably between channels; for tunnels charted in SFR, the flow-rate distribution is shown in Table I.

Calculations were made using the relative SFR flow-rate distribution applied to the conditions at the uranium mine.

If there was no erosion and the channels extended ad infinitum with the same flow-rate, the rate of movement of the tip of the redox front decreases inversely with the square root of time. This means that, for a constant rate of erosion, there will be a time at which the front moves as fast as erosion takes place, i.e. a steady state is achieved. This is shown in Figure 3.

Figure 3 shows the oxidised length along a channel for channels with low flow, categories IV – VIII. For example, the stationary length is 0.2 km for channels in category

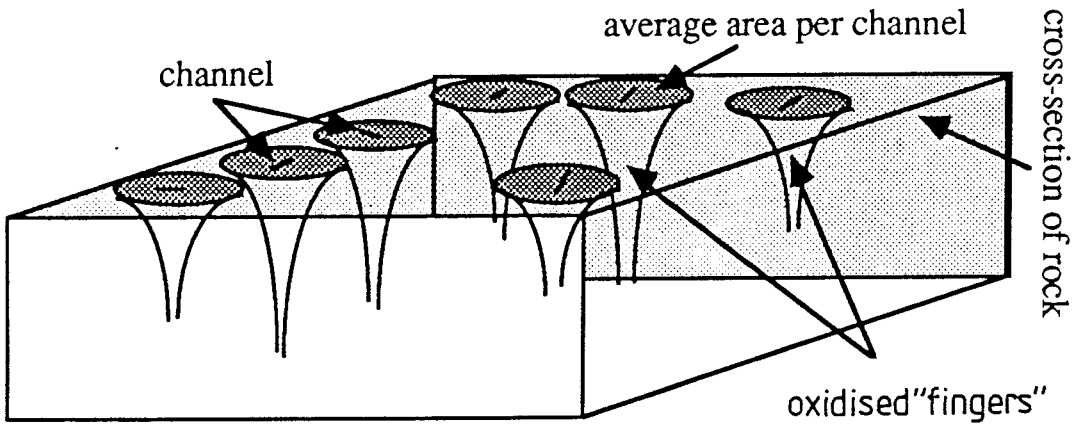

Figure 2. Cross-section of rock with independent channels.

TABLE I

Fraction of the total flow-rate which flows in different categories of channels. The data are from SFR in a mapped area of 14000 m^2. Categories VII and VIII are extrapolated for use at the Osamu Utsumi mine.

Channel category	Relative flow-rate	Fraction of spots	Fraction of flow-rate	Flow-rate per channel in Osamu Utsumi.* $m^3/s * 10^6$
I	32	0.012	0.131	2.758
II	16	0.024	0.148	1.550
III	8	0.073	0.207	0.723
IV	4	0.250	0.305	0.312
V	2	0.232	0.126	0.138
VI	1	0.409	0.084	0.052
VII	1/2			0.026
VIII	1/4			0.013

*These values give an average flow-rate of 100 l/m^2 a equivalent to 100 mm/a rainfall infiltration excess.

VI. The fastest channels would extend many kilometres if they were isolated. Even assuming that these channels are horizontal for long distances, the distance is too long to be reasonable, even accounting for erosion.

The above calculations were based on the assumption that channels extend ad infinitum with the same flow-rate along them for all time. This is not a reasonable assumption because of the "network" structure of channels.

It is seen from Figure 3 that, for channels with low flow (categories VI-VIII), the redox front in independent channels would stabilise at 20–200 m below the constantly eroding ground surface. For the channels with larger flow-rates, the length of the oxidised channels would become very large. It is conceivable that channels would keep their identity for tens to hundreds of metres if the channels are sparse. For greater distances, the channels are bound to intersect other channels and form a network. This would lead to a mixing of waters in different channels, causing the channels to lose their identity. The fronts would not penetrate as far as the individual channel concept would indicate.

Furthermore, the hydrologic modelling shows that the flow-rate at greater depths will decrease and also become more horizontal before finally turning upwards (Holmes *et al.*, this report series; Rep. 5). Very long channels will thus curve upwards to the surface.

The frequency of channels found in Swedish crystalline rocks was in the order of 1/20 m^2 to 1/100 m^2 and the frequency of redox fingers at the Osamu Utsumi mine was in the order of 1/1000 m^2. At the Osamu Utsumi mine, the fingers in the excavated rock could not be reconstructed; this results in a figure that is truncated and gives too few channels.

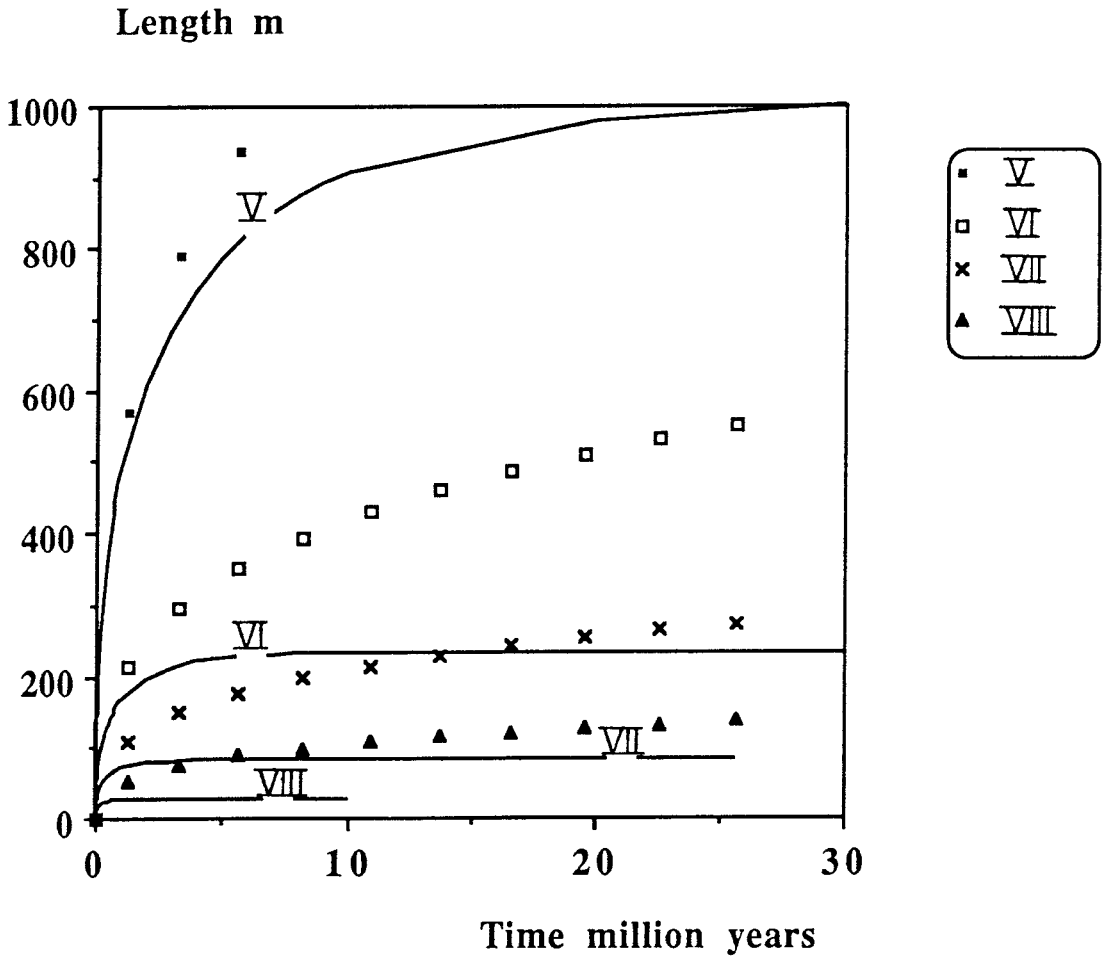

Figure 3. Length of oxidised "finger" as a function of time, either considering no erosion (symbols) or considering erosion (full lines) for independent channels of a given category (cf Table I).

Because the resolution of the mapping used is very coarse, finer channels will not be identified. Visual observations in the vertical walls show many more fine channels but these have not been quantified.

4. Chemical equilibrium modelling

First attempts to simulate the development of the redox front using an approach which considered both solute transport and local equilibrium (using a chemical thermodynamic model) were carried out at the Royal Institute of Technology, Stockholm. These studies used the computer codes CHEMTRN and TMCL, but considerable problems were encountered. In general, convergence was not obtained because of the shock-wave behaviour of the moving fronts.

Subsequent attempts to simulate aspects of the geochemical evolution of the redox front with chemical equilibrium models were carried out by independent groups at Harwell and Atkins, and are described in Sections 4.1 and 4.2 respectively. Section 4.3 attempts to compare these models and the extent to which they simulate reality.

4.1. Harwell modelling

J.E. Cross, A. Haworth, I. Neretnieks, S.M. Sharland and C.J. Tweed

The rock is assumed to act as a homogeneous porous medium, initially in reduced form throughout, with rainwater infiltrating from the ground surface. In the model, the flow is assumed to have a constant velocity along the flow path. It is assumed to be saturated with oxygen in equilibrium with air, and to have a concentration of carbon dioxide about one order of magnitude higher than the air equilibrium value, to match with the observed carbonate content in the waters. Such increased levels are assumed to result from the degradation of organic material in the soil covering the rock. The infiltration rate of the water is taken to be 0.1 $m^3m^{-2}year^{-1}$, which is about 5% of the rainfall in the area, 1.7 $m^3m^{-2}year^{-1}$ (Lei, 1984).

The pyrite content of the reduced rock is approximately 2% by weight, which is equivalent to 2.3 moles per litre of pore-water, assuming a porosity of 15%. The content of potassium feldspars is 70% by weight, which is equivalent to 35.2 moles similarly expressed per litre of pore-water in the oxidised rock. The formula of this mineral is

taken to be $KAlSi_3O_8$. Similar calculations for the amount of kaolinite and uranium in the system give values of 7.4 and $1.8x10^{-3}$ moles per litre respectively. The rest of the rock minerals are treated as inert. The data used for calculations are summarised in Table II. Sensitivity tests were performed to investigate the spatial discretisation in the model. Twenty cells are considered to be optimal in terms of numerical accuracy and computational efficiency.

TABLE II
Summary of input data for model.

Transport Parameters	
Grid length	1.0 m
Number of cells	20
Dispersion length	0.1 m
Aqueous pore diffusion coefficient	$1.2x10^{-10}$ m^2s^{-1}
Darcy velocity	$2.9x10^{-9}$ m s^{-1}
Timestep	$4x10^5$ s
Initial Rock Composition	
Pyrite content	2.3 mol/l porewater
K-Feldspar content	35.2 mol/l porewater
Kaolinite content	7.4 mol/l porewater
Uranium content	$1.8x10^{-3}$ mol/l porewater
Infiltrating Water	
pH	5.1
pe	13.6
Total dissolved carbonate	$1.6x10^{-4}$ mol/l
Dissolved oxygen	$3.1x10^{-4}$ mol/l

Some preliminary calculations of the diffusive mode of uranium migration have also been carried out.

4.1.1. The CHEQMATE code

CHEQMATE (CHemical EQuilibrium with Migration And Transport Equation) (Haworth *et al.*, 1988) is a computer code developed to model the evolution of spatially

inhomogeneous aqueous chemical systems. Such systems are characterised by simultaneous chemical equilibrium and solute migration processes. The chemical part of the code is based on the PHREEQE program (Parkhurst *et al.*, 1985). This calculates the equilibrium water chemistry for a particular inventory of chemical elements and mineral phases. The transport part of CHEQMATE models one-dimensional diffusion, electromigration, advection and dispersion. The equations are solved using a finite-difference scheme by dividing the system of interest into a grid of cells. The chemistry and transport are iteratively coupled, so the timescales for chemical equilibria are assumed to be much shorter than those associated with the transport processes. CHEQMATE includes a mineral-accounting technique, so minerals can be precipitated or dissolved from the system as the calculation proceeds.

The version of CHEQMATE used in the present calculations uses an explicit timestepping method, and the maximum timestep is limited by the magnitude of the diffusion and dispersion. In this problem, where there are large masses of minerals with low solubility, the number of timesteps needed to exhaust the minerals in one cell of the grid will be excessively large (several hundred thousand). To avoid this problem, a scaling procedure is used; the concentration of all minerals is reduced by a factor of 10^4 and the number of timesteps reduced in proportion. Hence each timestep is equivalent to about 125 years, and the minerals are assumed to reach equilibrium with the aqueous phase over this period. The procedure is permissible as long as the total amount of element in solution dissolved in a particular cell is small compared to the amount of that element residing in the solid phase in that cell. Walsh *et al.* (1984) and Schlechter *et al.* (1987) have used this method to model the movement of sharp fronts, and recently Lichtner (1988) has explored this approach to formulate a solution procedure which is applicable to these situations.

The thermodynamic data used for these simulations was taken from the HATCHES (HArwell/Nirex Thermodynamic database for CHemical Equilibrium Studies) database. Details of this database are given by Cross and Ewart (1990). The uranium dataset is largely based on that recently published by Lemire (1988), but the anionic uranium (VI) hydrolysis species have not been included since recent uranium (VI) solubility studies at Harwell do not support their existence. However, since the pH in this system is about 8, these species would not be expected to form in any case.

4.1.2. Preliminary results from modelling

Figure 4 shows the location of the hydrolysis front, the redox front and the accumulation of uranium at the redox front at 300 timesteps in a rock column 1 m long. With the time scaling factor, this is equivalent to 38,000 years. The rock at depths greater than about 0.8 m (right-hand side of the figure) is not yet influenced by the infiltrating water. Behind the redox front (depths <8 m), all the pyrite has been oxidised to iron(III) minerals, represented by hematite in the calculation. The sulphide has been oxidised to sulphate and swept downflow out of the system. All the pitchblende/uraninite upflow of the redox front has dissolved and accumulated at the front.

The protons produced in the oxidising reaction have reacted with the K-feldspar to form kaolinite, releasing potassium and silica into solution

$$2\,KAlSi_3O_8(s) + 2\,H^+ + H_2O \Leftrightarrow Al_2Si_2O_5(OH)_4(s) + 2K^+ + 4\,SiO_2(s)$$

Behind the redox front, chalcedony has formed. Further upflow, at a depth of about 0.2 m, the hydrolysis front is formed; the K-feldspar has completely reacted to form more kaolinite and chalcedony. Some silica is also dissolved.

Figure 5 shows the composition of the solution phase. At the redox front, the pe drops from about 12 in the oxidised region to about -5 in the reduced region. The pH is constant at about 8.6 on both sides of the redox front, but decreases gradually to below 6 in the hydrolysed zone.

Figure 6 shows the concentrations of dissolved sulphate, carbonate, potassium and silica. The total carbonate concentration is almost constant through the whole grid, since it does not precipitate in any mineral phase. The other species increase in concentration from the inlet up to the point where they become controlled either by their solubility or by the reaction of a mineral phase; for example the oxidation of pyrite limits the supply of sulphate in the reduced region. Aluminium is present in very low concentrations in the solution (Fig. 5), in equilibrium with various minerals phases, whereas the more soluble components of the minerals, e.g. potassium and silica, dissolve.

Figure 7 shows the speciation of uranium in solution in the system. There is a clear switch from uranium (IV) to uranium (VI) species at the redox front. In the oxidised region, a mixture of hydrolysis and carbonate species are predicted, whilst in the reduced region the predicted speciation is completely dominated by the uranium (IV) hydrolysis product $U(OH)_4^\circ$. This change in speciation is also reflected in the total soluble uranium concentration. In the reduced region, uranium is predicted to be at a level of about 10^{-10}

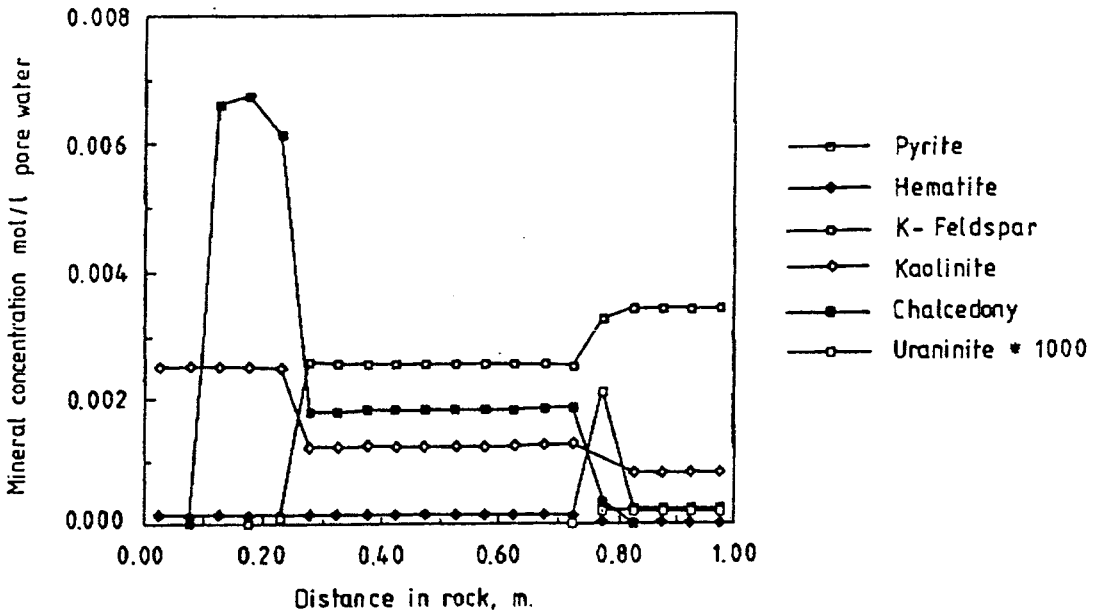

Figure 4. Predicted mineral concentrations with depth at 38,000 years (assuming mineral scaling in calculation).

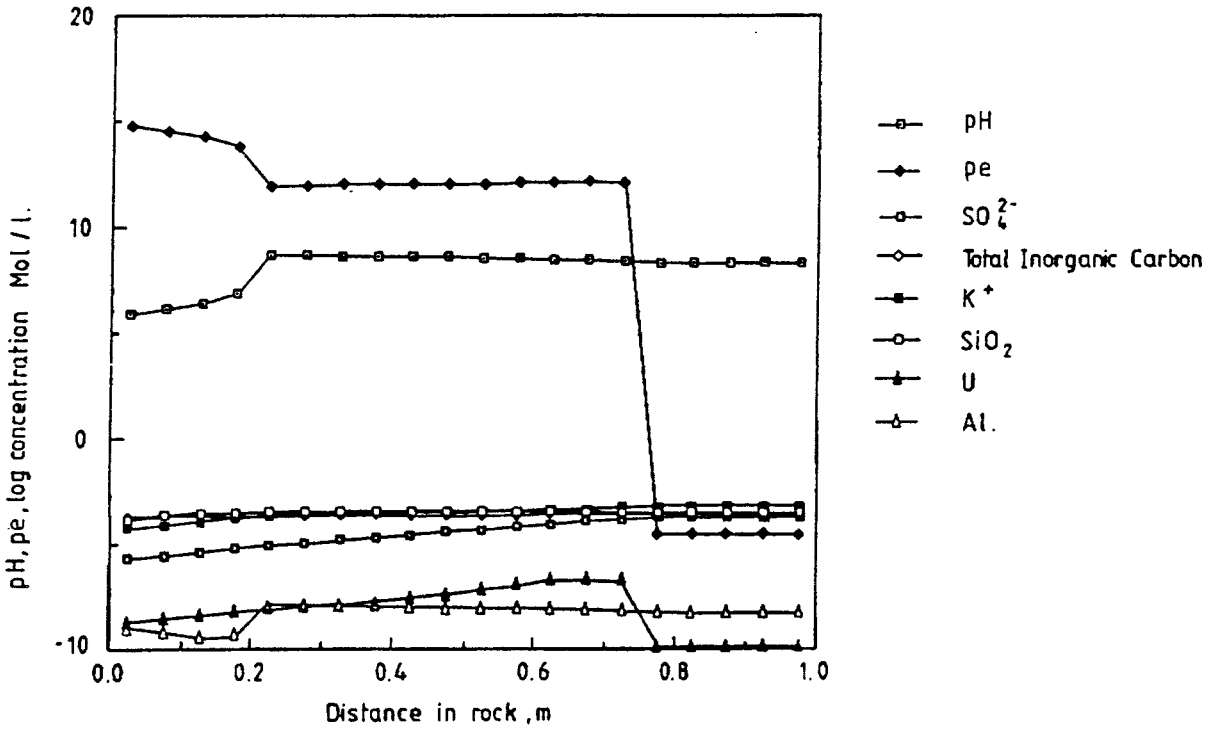

Figure 5. Predicted profiles of pH, pe and concentrations of various aqueous species at 38,000 years.

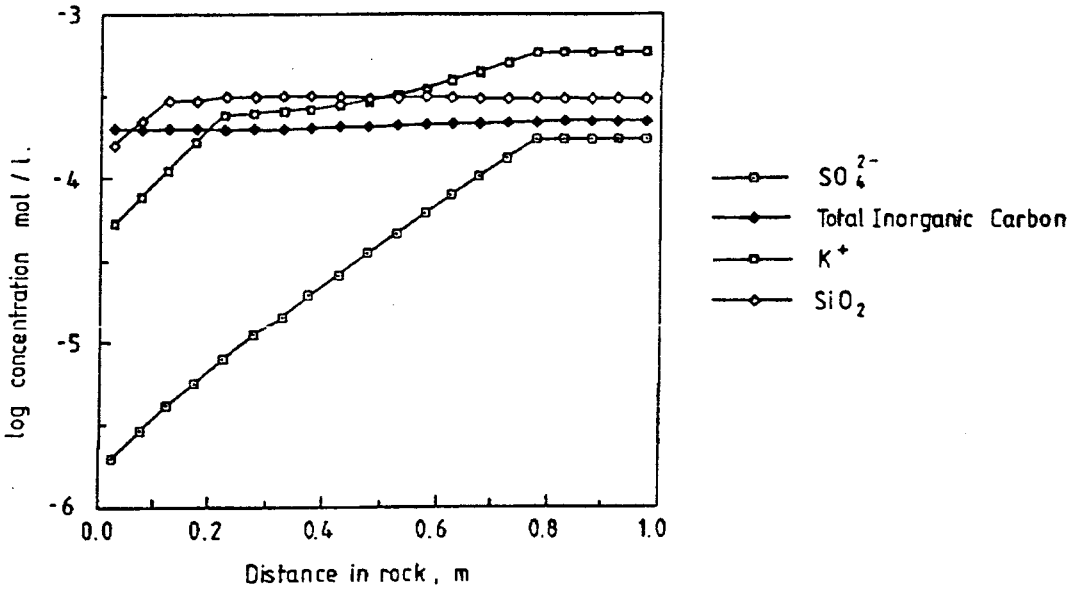

Figure 6. Predicted profiles of aqueous sulphate, carbonate, potassium and silicate at 38,000 years.

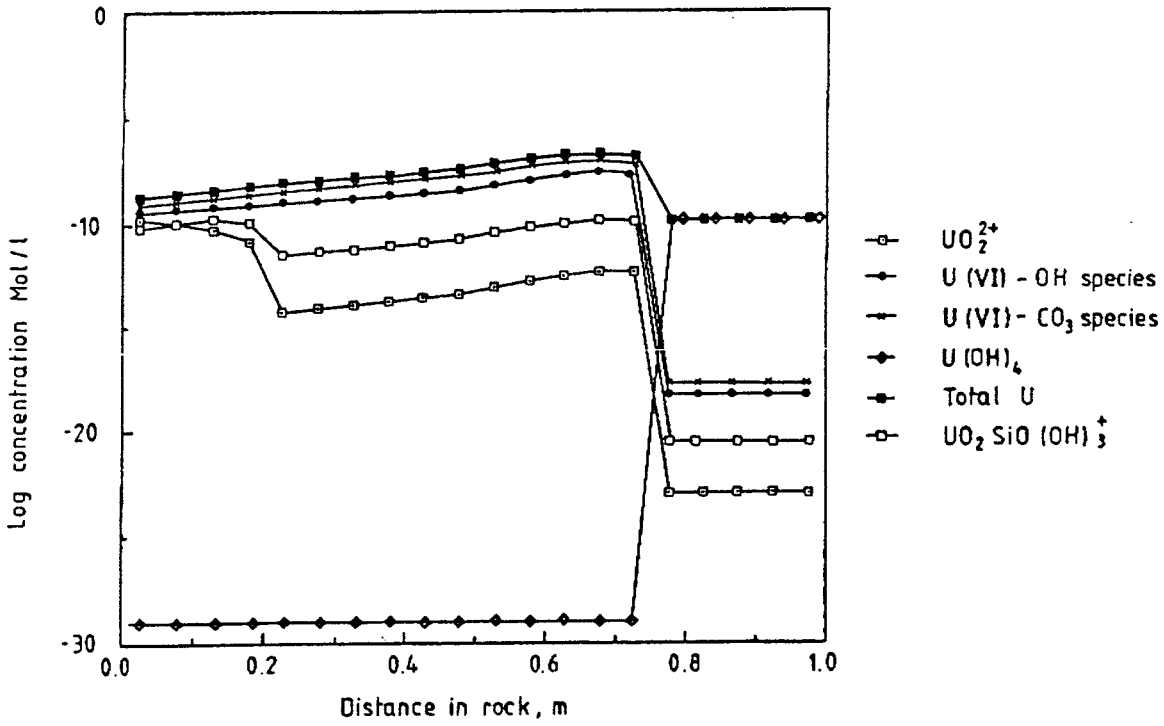

Figure 7. Predicted chemical speciation of uranium at 38,000 years.

M, controlled by the uraninite mineral phase. However, in the oxidised region, the uranium concentration is not solubility-controlled, reflecting the higher solubility of uranium (VI).

The above results were obtained assuming that the flow was evenly distributed as in a porous medium, and that the transport was dominated by advection. An effective Peclet number of 10 was used, which indicates that local transport by diffusion/dispersion contributes about 10% to the total.

Some preliminary calculations were also performed for a case with transport by molecular diffusion only. The results are shown in Figures 8 and 9 for 1.25×10^6 years (corrected for the scaling factor). Figure 8 shows the mineral content and Figure 9 shows some of the species concentrations, pH and pe. A redox front and hydrolysis front develop as in the advective case, but the uranium which precipitates at the redox front only accounts for about half the uranium which was originally present in the rock. The reason for this is that the model has simulated a case where water flushes past the surface of the rock, as in a fracture, and transport in the rock matrix takes place only by diffusion. The uranium dissolved at the redox front partly diffuses towards the face of the fracture, where it is swept away downstream by the water which contains little uranium. Also, the accumulation of chalcedony is smaller compared to the advective case for the same reason. The two small increases in the amounts of kaolinite and chalcedony around the redox front do not exist in the advective case. However, the results from the diffusive mode calculations may be considerably more sensitive to the numerical technique employed in solving the equations.

4.1.3. Discussion and preliminary comparisons with field data

The components which are generated by rock/water interaction and are not present in the inflowing water (for example, K^+, SO_4^{2-}, U etc.) will be subject to two competing processes, i.e. diffusion and dispersion upstream, or movement downstream swept in the flow. At steady state, the two rates of movement will balance the rate of supply. Steady state will prevail if the rate of movement of the front is small compared to that of the dissolved species. The following equation then applies:

$$\ell n\,(C/C_0) = (U\,(x-x_0))/D_e$$

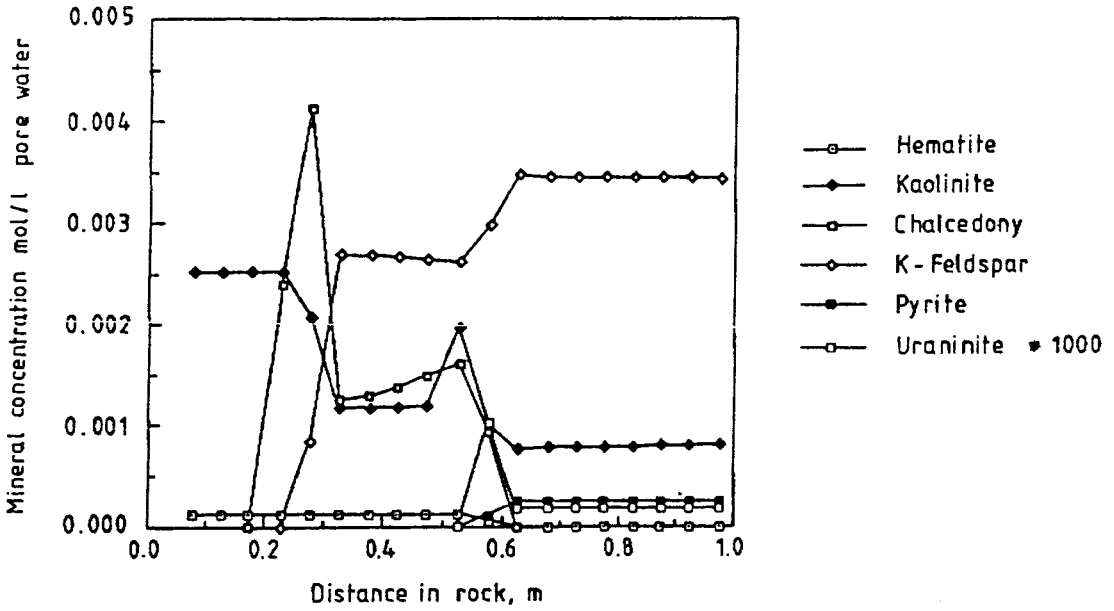

Figure 8. Predicted mineral concentrations with depth at 1.25x10^6 years for the diffusion only case.

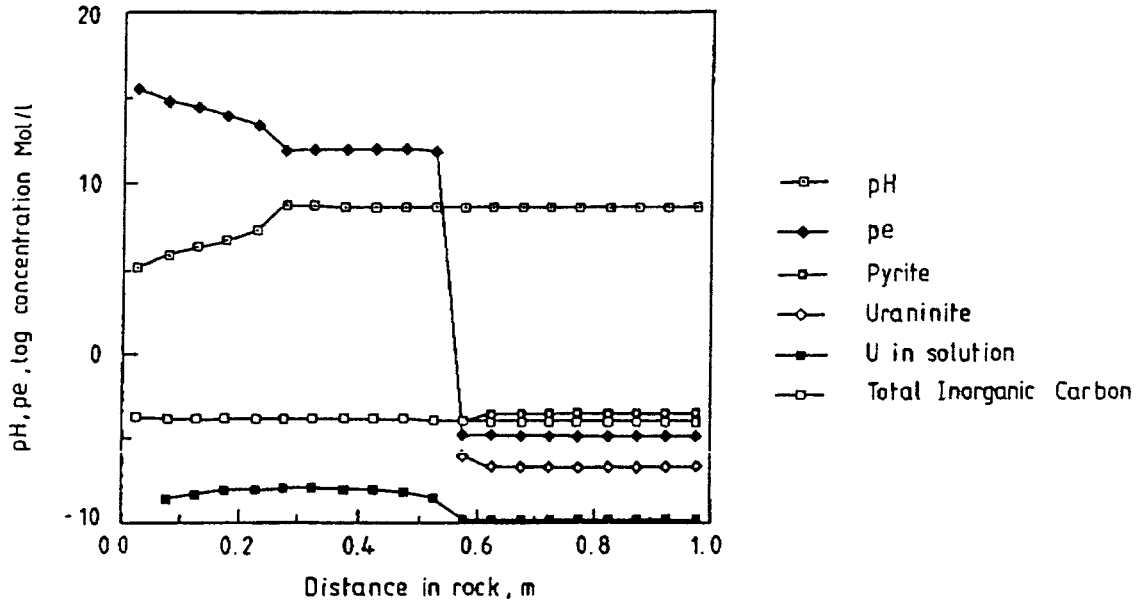

Figure 9. Predicted profiles of pH, pe and concentrations of various aqueous species and minerals at 1.25 x10^6 years (diffusion only).

where C_o is the concentration of the species in equilibrium with the solid phase, C is the concentration at depth x, U the Darcy velocity, D_e is the dispersivity and x_o is the depth of the first trace of the solid. The logarithm of the concentration versus distance should therefore be a straight line with slope U/D_e. The predicted sulphate, potassium and silica concentration profiles are indeed straight lines where there is no solid phase present, and the slopes give between 6.2 and 7.6 compared to 6.4 for the Peclet number (U/D_e). This supports the assumption that a steady state is achieved and the method of time scaling through the mineral quantities is reasonable.

Table III shows both field data and data obtained from the calculations of pH, pe and the solute concentration of some key components. The sulphate concentration agrees well with measured values. This is an indicator that the primary oxidation reaction of pyrite with dissolved oxygen is correctly assessed. The protons formed in this oxidation reaction react with the K-feldspar to release potassium. In addition, potassium is released at the hydrolysis front at about the same rate. The calculated potassium concentration is about a factor of two higher than the observed value. This discrepancy could be due to a number of factors. Some of the potassium may not be released, but bound in some intermediate mineral between the K-feldspar and kaolinite, e.g. illite, which is abundant in both the oxidised and reduced region in the rock. The K-feldspar-proton reaction also releases silica. The calculated silica concentration is about a factor of two lower than the observed values. In the model, the silica is precipitated as chalcedony. No pure silica minerals of comparable quantities are found in the field, and it must be concluded that this reaction does not take place as predicted.

TABLE III

Water chemistry calculated and observed just downstream (reduced) and upstream (oxidised) of the redox front.

	Reduced region		Oxidised region	
	Field	Calculated	Field	Calculated
pH	5.5–6.1	8.3	5.6-6.2	8.4
pe	1.3–5.5	-4.68	–	12.1
U (mg/l)	$(<3–4.5)\times10^{-3}$	0.03×10^{-3}	$(0.7\text{-}120)\times10^{-3}$	32.1×10^{-3}
SO_4^{2-} (mg/l)	9-20	16.8	10-300	12.9
K (mg/l)	8-13	22.7	–	19.6
SiO_2 (mg/l)	29-37	18.6	–	18.7

Comparison of the calculated uranium concentration with the field measurements shows quite good agreement in the oxidised region, where the calculated value falls well within the range of field values. However, in the reduced region, the predicted value is significantly lower than that observed. A possible reason for this discrepancy is that the uranium concentration is controlled by a more amorphous uranium(IV) hydroxide (pitchblende) solid phase, which is observed in the field, rather than the uraninite assumed in the model.

The model predicts pH 2 to 3 units higher than the field results. Several tests were performed to investigate if the formation of other clay minerals such as muscovite or other silica phases, including quartz and amorphous silica, would lead to significant changes in pH, but it was only possible to obtain minor differences in pH. The discrepancy could have several causes. A water of pH 8.3 would need only 1% contamination with water of pH 4 to obtain a pH of 6, and only 0.1% of a water with pH 3 to obtain the same result. Surface waters in the mine have been found to have pH 3.0–3.6. It is not inconceivable that sampling in boreholes by pumping may draw in small quantities of surface waters. This possibility is also suggested by the observed pe of + 3.2 to + 5.5 found in water samples in the reduced region. Another possibility is that the proton-K-feldspar reaction is kinetically hindered, and that the sample waters are not in equilibrium with the minerals. If it is assumed that the proton-feldspar reaction is only 99% complete, this would result in a pH of 5.5 as opposed to the value of 8.3 predicted for the complete reaction. Reaction rates estimated from kinetic data given in Lichtner (1988) suggest that such depletion might take from days to years, depending on the available surface area of the feldspar for reaction. This could be the case if the water samples were obtained from fractures where the exposed rock surface area for reaction is considerably smaller than when the flow takes place through the matrix of the rock. Both hypotheses are possible and, based on previous evidence for clay buffering at pH 8-8.5 (Lichtner *et al.*, 1987), it is felt that the modelling represents this aspect of the system correctly.

The calculations predict that, at time 38,000 years, the redox front is at a depth of about 0.8 m and the first hydrolysis front at 0.25 m (assuming the mineral scaling approximation described earlier). A second hydrolysis front is expected to form when the kaolinite is completely depleted of its silica, leaving aluminium oxide minerals such as gibbsite behind. The formation and movement of this front is much slower than that of other fronts, and the calculations have not yet been continued up to times where this front would appear. At the redox front, the K-feldspar is depleted and kaolinite forms. This transformation is directly proportional to the original concentration of pyrite. The

calculations show a 25% reduction in the feldspar content. This and the coupled increase of kaolinite content agrees well with the observed rock composition. The total depletion of pyrite and the formation of ferric oxyhydroxides also agree well with the field observations, as does the formation of a zone with enhanced pitchblende concentration at the redox front.

The rate of movement of the redox front was calculated to be 21 m per million years with the assumptions based on vertical water flow-rate, pyrite and dissolved oxygen concentration described in this section. The water flow-rate decreases with depth and may be as much as an order of magnitude different from that assumed in this calculation. Consequently, the movement of the redox front decreases with depth and the predicted rate may be in error by the same amount. However, within this range, there still appears to be a balance between the rate of erosion of the rock and the rate of movement of the redox front.

4.1.4. Conclusions

A study of the natural migration of uranium at the Osamu Utsumi uranium mine has been performed using the coupled chemical equilibria/transport computer code CHEQMATE. Preliminary results presented in this section give some encouraging agreements with field data. These include the rate of migration of the redox front and hydrolysis front, certain mineral transformation reactions and concentrations of various aqueous species in the system. This gives confidence in the validity of applying such modelling techniques to other problems associated with the migration of radionuclides away from a nuclear waste repository. For particular aspects of the problem where good agreement with field data was not obtained, a number of suggestions have been made for discrepancies. These include incorrect choice of solubility-limiting mineral phases in the model, mineral precipitation reactions not being at equilibrium, and possible errors in field measurements due to contamination of deep groundwater samples by surface waters.

4.2. Atkins modelling

D. Read

4.2.1. Observations used to derive the model

Three regions in the profile from the Osamu Utsumi mine may be distinguished (Waber *et al.*, this report series; Rep. 2). At shallow depths (<40 m) the rock has been completely argillised, the main products being kaolinite (63%) and illite (28%). Evidence of oxidation, however, may be found to depths of 200 m below surface where preferential groundwater ingress along a series of sub-parallel fractures has given rise to oxidised wedges arranged en echelon (Fig. 1). The dominant minerals in this variably weathered zone are potassium feldspar (50%), illite (21%) and kaolinite (17%), with ubiquitous iron oxyhydroxides. The underlying reduced zone has a similar feldspar/clay mineralogy to the oxidised zone, the main difference being the presence of accessory pyrite and fine-grained aggregates of pitchblende. Along the redox fronts themselves, pitchblende forms larger kidney-shaped nodules up to centimetre size and displaying signs of recrystallisation.

In terms of mean bulk rock chemistry there is little indication of net major element removal from the oxidised zone (Table IV). The same may be said of the majority of trace elements, though cerium shows a slight enrichment while the other rare-earths, zirconium and niobium show some depletion (<50%). Sulphur is a notable exception to the above, levels decreasing from about 1% in the reduced zone to less than 50 ppm as a result of pyrite oxidation. However, iron concentrations are only 6% lower in the oxidised rock and this, together with the remaining analyses (Table IV), points to substantial mineral transformation in situ.

The distribution of uranium and thorium along the profile is shown in Figure 10. Uranium concentrations decrease uniformly from the weathered zone to <10 ppm at a depth of 100 m below the surface. At greater depths, concentrations fluctuate markedly owing to the alternation of oxidised and reduced rock along a series of closely spaced fracture zones. Although the highest levels found (>3%) reflect pitchblende mineralisation in reduced rock, high concentrations are not confined to these regions. Elevated uranium concentrations have also been recorded in oxidised material where the uranium occurs in association with iron oxyhydroxides (Waber *et al.*, this report series; Rep. 2). Below 200 m uranium concentrations vary little around a mean of about 30 ppm (Fig. 10).

TABLE IV

Osamu Utsumi mine: mean bulk rock chemistry of leucocratic phonolites.

Element		Oxidised Zone n = 6	Reduced Zone n = 21	Weathered Zone n = 1
SiO_2	wt.%	55.74	56.89	36.12
TiO_2		0.53	0.44	0.66
Al_2O_3		23.28	21.80	33.66
Fe_2O_3(tot)		3.04	2.53	7.65
MnO		0.00	0.04	2.52
MgO		0.03	0.05	n.d.
CaO		0.00	0.19	0.00
Na_2O		0.29	0.36	0.18
K_2O		12.96	13.72	2.78
P_2O_5		0.07	0.06	0.12
LOI		3.27	3.08	13.69
CO_2		n.a.	n.a.	n.a.
F	ppm	1218	2085	
Ba		583	677	
Rb		315	309	
Sr		188	198	
Pb		30	4	
Th		46	30	
U		185	20	
Nb		225	188	
La		309	268	n.a.
Ce		673	311	
Nd		83	61	
Y		73	54	
Zr		1360	1009	
V		239	236	
Cr		7	6	
Ni		5	b.det.	
Co		6	5	
Cu		b.det.	b.det.	
Zn		24	222	
Hf		12	10	
Ga		40	38	
Sc		3	3	
S		27	8237	

n.a. = not analysed
b.det. = below detection limit
LOI = Lost on ignition

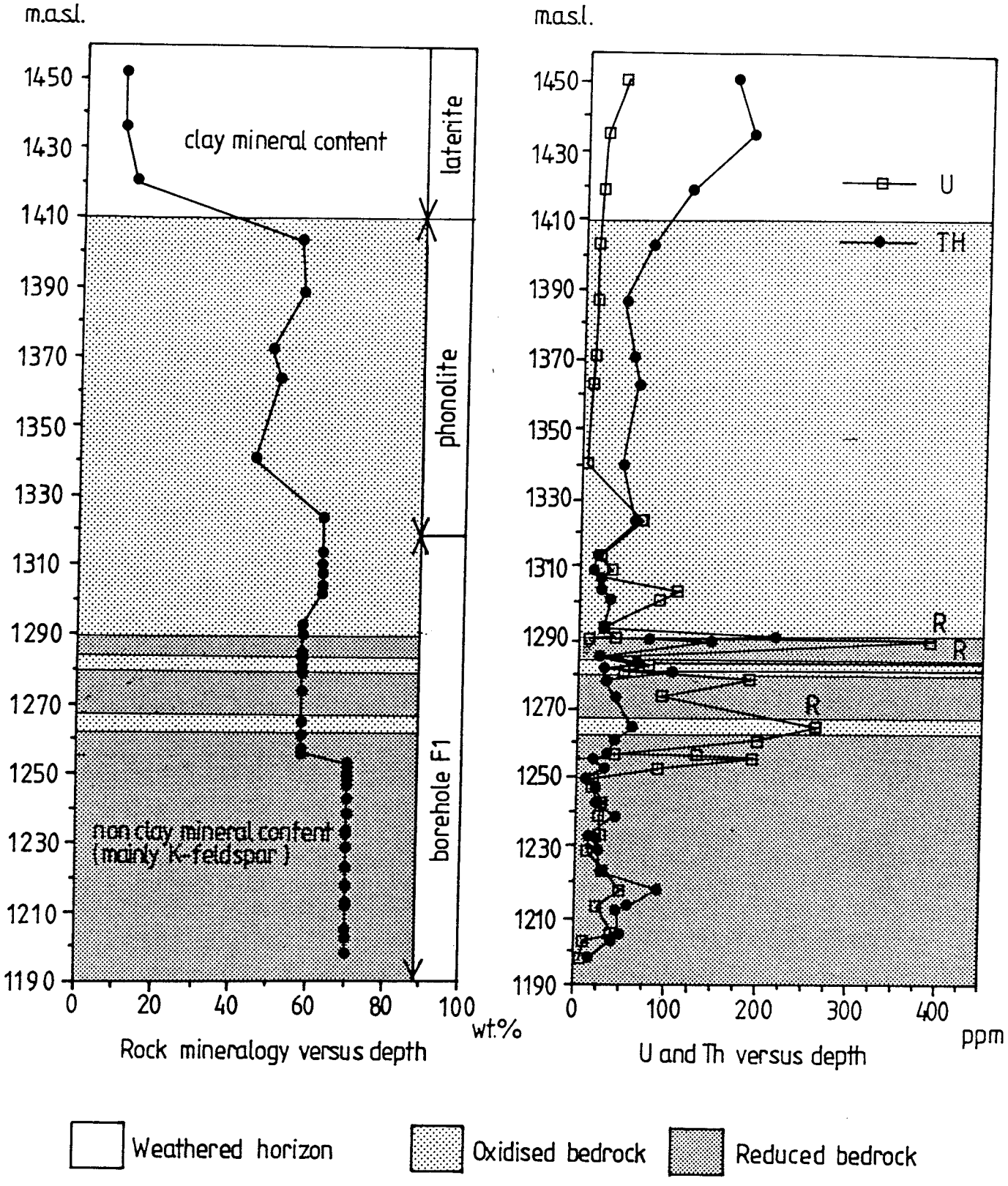

Figure 10. Distribution of clay mineral content, uranium and thorium with depth from the original (pre-mine) ground surface to the bottom of borehole F1. Note the distinct change in mineralogy at about 1414 metres above sea level (m.a.s.l.), and the enrichment of uranium and thorium at the surface and associated with the redox fronts (denoted by 'R').

The thorium profile is sub-parallel to that of uranium but accumulation in the uppermost weathered zone is more pronounced. The highest levels (190 ppm) are found some 15 m below the surface where lateritisation is advanced.

4.2.2. Conceptual basis of the model

It is apparent from Figure 10 that substantial mass transfer of uranium has occurred in the sequence studied at the Osamu Utsumi mine. However, the mechanisms by which this movement have been effected are complex and cannot be explained by a simple "roll front" process as suggested previously for uranium deposition in sandstone formations (Walsh *et al.*, 1984). The main objections to a model based solely on redox precipitation include the following:

- there is clear evidence of uranium deposition in both oxidised and reduced rock (MacKenzie *et al.*, this report series; Rep. 7),
- the depth profile of thorium, which is not redox-sensitive (Fig. 10),
- in terms of bulk rock chemistry, uranium is not depleted in the oxidised zone owing to significant retention on iron oxyhydroxides (Table IV),
- rare-earth element (REE) analyses for groundwaters from the region show marked cerium depletion, indicative of fixation under oxidising conditions (Miekeley *et al.*, this report series; Rep. 8). As with uranium, iron oxyhydroxides are the dominant sink,
- kinetically, the oxidation of pyrite is much faster than leaching of primary pitchblende ore (Posey-Dowty *et al.*, 1987). Progression of the oxidising front and uranium mobilisation – reprecipitation are unlikely to be contemporaneous,
- uranium series data (MacKenzie *et al.*, this report series; Rep. 7) show diffusion to have occurred in both directions across a redox front at 42 m depth in borehole F1. The results imply effectively zero net advection across the front over a period of up to 1 million years.

For modelling purposes, the Osamu Utsumi mine sequence may be considered in terms of several discrete geochemical environments, namely laterite (0-40 m), the oxidised zone (40–190 m), the reduced zone (>200 m) and the redox front itself. In this report, the oxidised region has been further subdivided into an upper zone of leaching (40-140 m) and one of accumulation (140–190 m).

The laterite zone is a region of intense weathering; an open system from which labile constituents have been selectively removed and resistates correspondingly enriched. It is not considered further in this report. Additionally, field evidence suggests that the reduced zone, below 200 m depth, may be regarded as a stable environment within which primary uranium ore persists (Waber *et al.*, this report series; Rep. 2). For these reasons, effort has been concentrated on the middle part of the section. Emphasis in modelling has been placed on leaching and subsequent fixation of uranium by iron oxyhydroxides, together with diffusion, reduction and precipitation across the redox front. Groundwater analyses taken to be representative of the leaching, accumulation and reduced zones are given in Table V.

TABLE V
Composition of groundwaters from the Osamu Utsumi mine (mol dm^{-3}).

	Oxidised Region		Reduced Region
	Leaching zone	Accumulation zone	
Na	$1.3x10^{-5}$	$4.3x10^{-5}$	$1.9x10^{-5}$
K	$2.9x10^{-4}$	$3.6x10^{-4}$	$2.8x10^{-4}$
Ca	$5.3x10^{-5}$	$3.1x10^{-4}$	$1.1x10^{-5}$
Mg	$2.9x10^{-6}$	$1.9x10^{-5}$	$2.5x10^{-6}$
Fe	$2.0x10^{-5}$	$7.6x10^{-5}$	$2.3x10^{-5}$
HCO_3	$1.6x10^{-4}$	$2.2x10^{-4}$	$1.9x10^{-4}$
SO_4	$1.3x10^{-4}$	$4.8x10^{-4}$	$1.7x10^{-4}$
Cl	$2.8x10^{-6}$	$5.5x10^{-5}$	$5.1x10^{-6}$
SiO_2	$4.8x10^{-4}$	$6.2x10^{-4}$	$5.0x10^{-4}$
U	$2.4x10^{-8}$	$2.8x10^{-7}$	$*1.0x10^{-10}$
pH	6.0	6.3	6.0
Eh(mV)	300	300	*-350

*Value assumed in chemical transport modelling.

The data used are among the most complete water analyses obtained from the Osamu Utsumi mine. The reported pH values are assumed to be accurate, despite possible sampling difficulties (section 4.1.3), but the probe Eh measurements are at best a semi-quantitative guide to the prevailing redox conditions. Given this uncertainty, a value of + 300 mV (pe ~5) has been adopted for modelling of the oxidised zones (Bruno *et al.*, this report series; Rep. 11). An Eh of -350 mV (pe ~-5.8) was assumed for the

reduced rock, in the absence of a direct measurement, consistent with the known stability of pyrite and pitchblende.

In summary, the conceptual model for uranium mobilisation may be formulated as follows:

i) Percolation of oxygenated waters through the profile; rapid conversion of pyrite to iron oxyhydroxides.

ii) Slower dissolution of primary pitchblende ore; release of U(VI) species to solution.

iii) Fixation of U(VI) hydroxy and hydroxy-carbonate species (Bruno *et al.*, this report series; Rep. 11) by iron oxides.

iv) Diffusion and reduction across fracture-controlled redox interfaces; localised redistribution of uranium and formation of secondary pitchblende ore.

This postulated sequence of events has been modelled using the CHEMTARD code (Liew and Read, 1988) and the CHEMVAL Stage 3 thermodynamic database (Read *et al.*, 1990). The latter was supplemented, where necessary, with recent uranium data from Lemire (1988). Results are summarised in the following sections.

4.2.3. Fixation of uranium in the oxidised zone

The oxidised region in the Osamu Utsumi mine extends for 150 m below the laterite "crust". As noted previously, this may be subdivided into the upper 100 m, where uranium concentrations are fairly constant at about 10 ppm, and the lower 50 m where concentrations range up to 400 ppm (Fig. 10). Given that the mean uranium level in the oxidised region as a whole is 50 ppm (Table IV), 130 ppm would seem a reasonable mean value for the accumulation zone. This raises the question as to whether the mine profile can be regarded as a closed system and, further, whether the redistribution of uranium in the oxidised zone can be explained solely by adsorption onto iron oxides. There are few sinks for uranium other than iron oxyhydroxides. The association with organic carbon is far less pronounced (Waber *et al.*, this report series; Rep. 2) and, in contrast to uranium occurrences elsewhere (Duerden, 1990), there is no apparent correlation with phosphate. The results of recent sequential extraction experiments confirm the importance of the ferric oxide association (Waber *et al.*, op. cit.; Appendix 2).

The amount of uranium removed in a 100 m vertical section of unit cross-sectional area is roughly 5 kg or 21 moles. Assuming that the rock prior to alteration contained a uniform 30 ppm U, the net addition of 21 moles to the accumulation zone would produce a mean rock concentration of 80 ppm. This is towards the lower end of the concentration range found, indicating some contribution from what is now the laterite zone. Nevertheless, such calculations suggest that, as a first approximation, the system may be regarded as closed.

A series of simulations were performed to quantify the abstraction of uranium by hydrous iron oxides. As a first stage, the speciation of uranium in the leaching and accumulation zones was estimated using PHREEQE (Parkhurst *et al.*, 1985) and the CHEMVAL Stage 3 database (Read *et al.*, 1990). The results are presented in Bruno *et al.* (this report series; Rep. 11). Uranium (VI), hydroxy, carbonate and hydroxy-carbonate species dominate, the relative proportion being dependent on absolute uranium levels. Further, predicted solubility in both samples far exceeds measured uranium, consistent with strong leaching and the absence of pitchblende in the zone above the redox front (Waber *et al.*, op. cit.). Parallel calculations performed with a thermodynamic database compiled at Harwell give close agreement in predicted solubility, with $(UO_2)_3(OH)_5^+$ the dominant complex (Bruno *et al.*, op. cit.).

Adsorption of uranium species was simulated using the Triple Layer Model (TLM) (Davis and Leckie, 1978) and supporting data compiled for the UK Department of the Environment radiological assessment programme (Economides *et al.*, 1989). Briefly, the model considers a neutral surface (SOH) which can dissociate to give a negatively charged site:

$$SOH = SO^- + H_s^+ \qquad \text{(i)}$$

where the subscript denotes an ion located at the surface plane

or, conversely, can react with a proton at the surface to form a positively charged site:

$$SOH + H_s^+ = SOH_2^+ \qquad \text{(ii)}$$

The activity of the proton in the surface plane is related to that in the bulk solution by:

$$aH_s^+ = aH^+ \exp\left(\frac{-e\,\psi}{kT}\right) \qquad \text{(iii)}$$

where ψ is the change of potential when a species moves from the bulk solution to the solid phase, e is the electronic charge, k is the Boltzmann Constant and T the absolute temperature.

The current version of the database contains specific adsorption constants for mono-, bi- and tri-dentate binding of $(UO_2)_3(OH)_5^+$ onto goethite and amorphous $Fe(OH)_3$. Only monodentate complexation was considered in this work. No data are available for $(UO_2)_2CO_3(OH)_3^-$, however, and values were obtained by analogy with univalent $UO_2(OH)_3^-$ (Kent *et al.*, 1986). Sorption equilibria considered are summarised in Table VI.

TABLE VI
Intrinsic equilibrium constants for sorption onto α FeOOH.

Reaction	logK
$SOH + Ca^{2+} \Leftrightarrow SO\text{-}Ca^+ + H^+$	-5.0
$SOH + Mg^{2+} \Leftrightarrow SO\text{-}Mg^+ + H^+$	-5.5
$SOH + Na^+ \Leftrightarrow SO\text{-}Na + H^+$	-8.4
$SOH + K^+ \Leftrightarrow SO\text{-}K + H^+$	-8.4
$SOH + H^+ + Cl^- \Leftrightarrow SOH_2\text{-}Cl$	7.0
$SOH + H^+ + HCO_3^- \Leftrightarrow SOH_2\text{-}HCO_3$	12.0
$SOH + H^+UO_2(CO_3)_2^{2-} \Leftrightarrow SOH_2\text{-}UO_2(CO_3)_2^-$	13.0
$SOH + (UO_2)_3(OH)_5^+ \Leftrightarrow SO\text{-}(UO_2)_3(OH)_5 + H^+$	0.66
$SOH + H^+ + (UO_2)_2CO_3(OH)_3^- = SOH_2(UO_2)_2CO_3(OH)_3^-$	7.0

Surface deprotonation constants used in the modelling study were 4.5 (pK1) and 12.0 (pK2). Auxiliary thermodynamic data taken from Read et al. (1990) and Hsi and Langmuir (1985).

The uptake of $(UO_2)_3(OH)_5^+$ and $UO_2(OH)_3^-$ respectively was modelled as a function of pH and properties of the solid surface, principally surface area and the effective concentration of surface sites. The results for $(UO_2)_3(OH)_5^+$ are shown in Figures 11 and 12.

As the model is based on equilibrium partitioning, the concentration of uranium sorbed increases in line with aqueous levels and thus, with all other parameters constant, sorption in the accumulation zone is roughly four times that in the upper zone of leaching (Fig. 10). Naturally, sorbed concentrations also increase markedly with solid surface area and the density of surface sites. As no direct data are available for these parameters from Poços de Caldas samples, sensitivity studies have been carried out for the range reported in the TLM database (Economides *et al.*, 1989). Given the abundance of iron oxides,

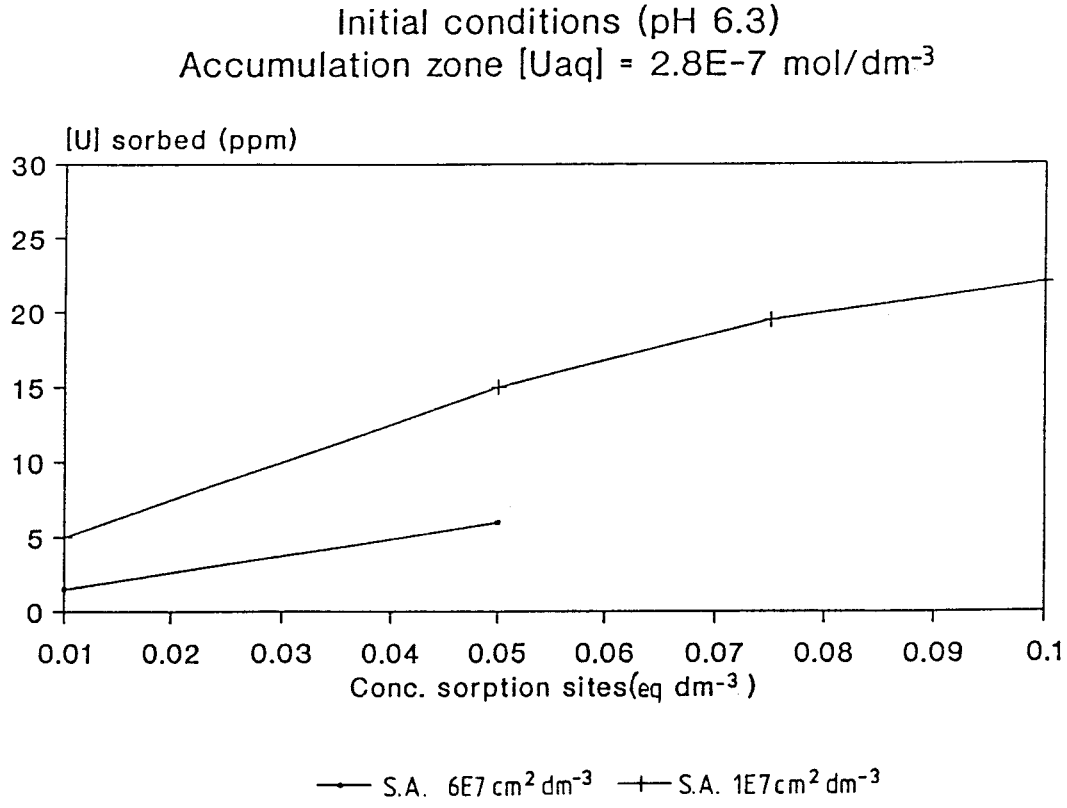

Figure 11. Sorption of $(UO_2)_3(OH)_5^+$ on αFeOOH as a function of surface area (S.A.) and concentration of surface sites.

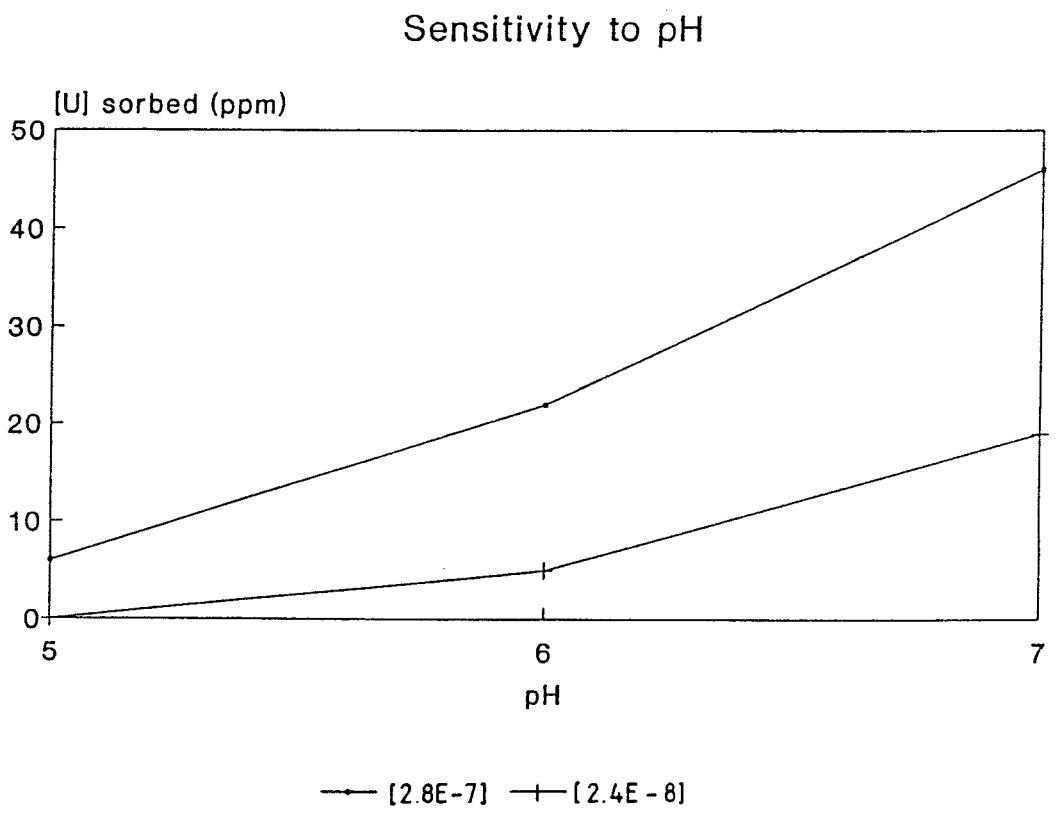

Figure 12. Sorption of $(UO_2)_3(OH)_5^+$ on α FeOOH (sensitivity to pH).

however, (Table IV) and their occurrence as finely dispersed coatings, the higher estimates are probably more representative.

It is apparent from Figures 11 and 12 that adsorption in the accumulation zone is of the right order to account for the levels observed. The predicted pH-dependence (Fig. 12) may explain in part the vertical distribution of uranium in the oxidised profile as deeper waters might be more alkaline (cf section 4.1.3). This effect is likely to be enhanced by the greater "ageing" of oxide phases in regions far above the present redox front.

In summary, predicted sorption of cationic U(VI) hydroxy species on amorphous iron oxides approaches the levels observed in the Osamu Utsumi mine and reinforces simple mass balance calculations of uranium redistribution in the oxidised zone. Corresponding simulations performed for anionic $UO_2(OH)_3^-$ indicate only weak binding at the ppb level. Scavenging of such complexes is regarded as making relatively little contribution to the total amount of uranium removed from the groundwaters.

4.2.4. Transport of uranium across the redox front

Whereas specific adsorption of U(VI) complexes onto ferric hydroxide may account for uranium retention in the oxidised zone, precipitation of secondary pitchblende is clearly occurring at the redox front itself (Waber *et al.*, this report series; Rep. 2). Uranium concentrations of up to 3% have been measured in whole-rock analyses as a result of concretionary nodule formation in reduced rock.

Coupled chemical transport calculations have been performed in an attempt to simulate the reduction and precipitation of uranium across a zone encountered at 42 m depth in borehole F1, one of the most intensively mineralised redox fronts studied in detail at the Osamu Utsumi mine. Again the CHEMTARD code was used with data from CHEMVAL and Lemire. Groundwater at an Eh of + 300 mV and containing a uranium concentration typical of the deeper oxidising zone (Table V) was allowed to diffuse into reducing rock at an Eh of -350 mV. Only pure diffusion of aqueous species was considered in view of strong evidence that net vertical flow across the front has been effectively zero for the past million years (MacKenzie *et al.*, this report series; Rep. 7). Advective transport along fractures parallel to the front is likely, however, and has been suggested (cf section 4.1.3) as a means by which uranium could be concentrated at the tips of "redox wedges". As pitchblende nodules are not generally found in such locations, the effects of lateral dispersion have been ignored in this work.

A 2 m domain length was considered with diffusion occurring over a period of 1 million years. Although this timescale may be short in comparison to the evolution of the deposit as a whole, it represents a reasonable estimate of the time for which hydrologic conditions at the front have remained stable (MacKenzie *et al.*, this report series; Rep. 7). The analytical data were those employed in earlier speciation/solubility calculations (Table V). Sensitivity analyses were performed to account for the uncertainty in uranium diffusion rate, estimated as between 10^{-10} and 10^{-13} m^2s^{-1}.

As a first stage, equilibration with solid phases was omitted in order to provide an indication of the saturation state of U(IV) and U(VI) minerals along the diffusion profile. Figure 13 plots saturation indices (log ion activity product/solubility product) for uraninite (UO_2) and schoepite ($UO_2(OH)_2$) at 1 m from the source, assuming a pore diffusion coefficient of $10^{-13}m^2s^{-1}$. A value of zero on the ordinate would represent exact saturation with respect to that mineral. It can be seen that, even at such low diffusion rates, uraninite rapidly becomes supersaturated on entering the reduced rock. Schoepite and other U(VI) phases do not approach saturation despite increasing levels of uranium emanating from the boundary (Fig 13). This points to the dominating effect of reduction and the stability of $U(OH)_4^\circ$.

The above calculations suggest uraninite to be supersaturated throughout the profile but provide no indication of the likely disposition of uranium within the reduced rock. Thus, in subsequent simulations, deposition from solution was permitted, allowing mass transfer of uranium to be monitored as a function of distance and time.

The effect of uraninite precipitation on elemental solubility is apparent from Figure 14. Aqueous concentrations fall by more than three orders of magnitude over a distance of 5 cm. Correspondingly, speciation changes from U(VI) hydroxy and hydroxy-carbonates (Bruno *et al.*, this report series; Rep. 11) to $U(OH)_4^\circ$. At distances greater than 10 cm beyond the front, uranium levels are constant at 10^{-10}mol dm^{-3}.

The build-up of uraninite in the reduced zone may be quantified and used to provide a mass balance for uranium transfer. Effective concentrations of uraninite precipitated per dm^3 of pore-water are shown in Figure 15 for a range of diffusion coefficients. Three points in particular are worthy of note.

i) Uraninite precipitation is localised at the first space node within the reduced domain. Increasing the mass of uranium diffusing into the field causes a build-up of solid at this node rather than progressive deposition down-gradient.

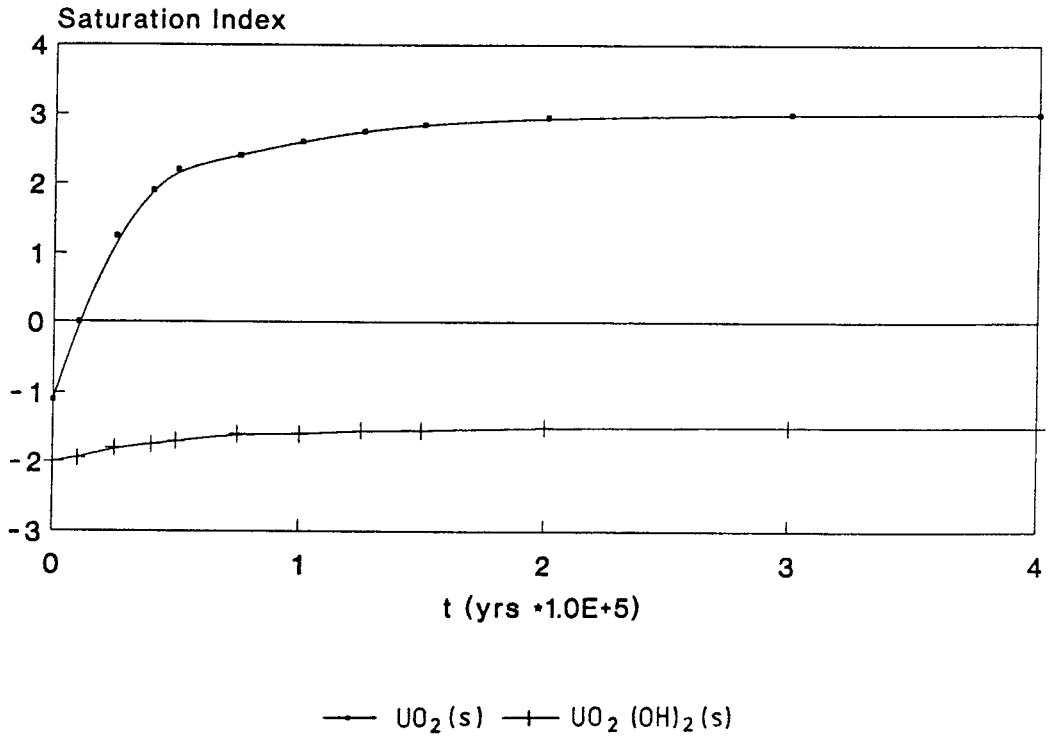

Figure 13. Saturation state of uraninite and schoepite (profile versus time at x=1m).

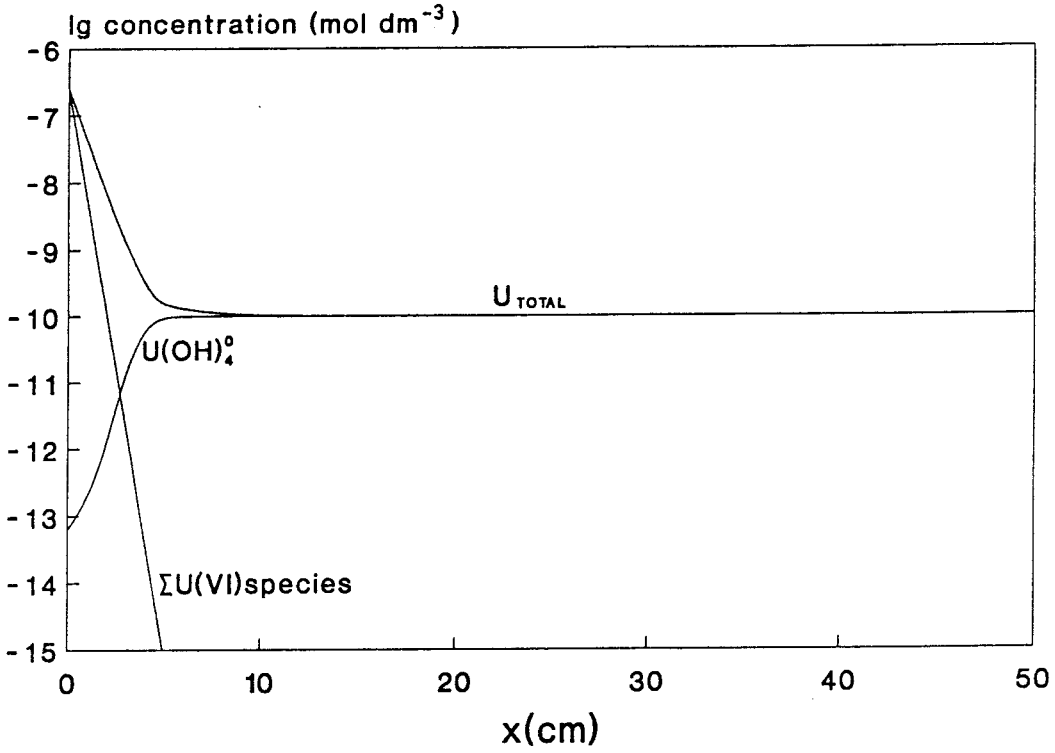

Figure 14. Change in uranium concentration across the redox front at $t = 10^6$ y.

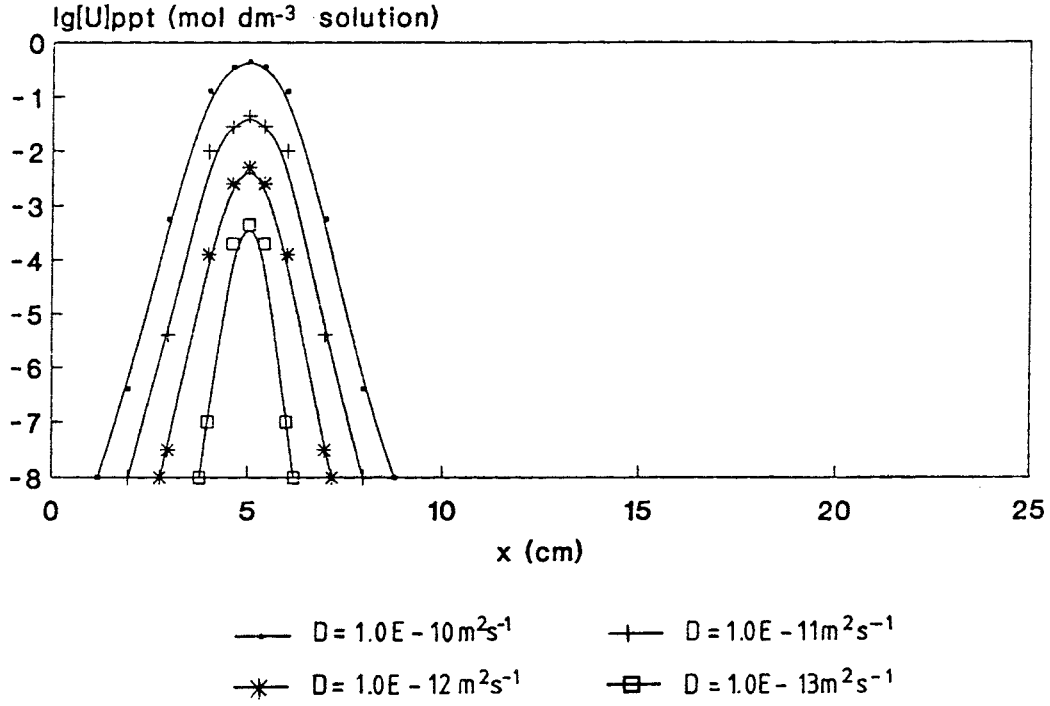

Figure 15. Precipitation of uranium at the redox front at $t = 10^6$ y for different values of the diffusion coefficient for U (D).

ii) The redox front itself is stationary over the study period. In the absence of advective flow, the Eh beyond 10 cm into the calculation domain is unaffected by oxidising conditions at the boundary.

iii) For higher diffusion coefficients, the concentration of uranium precipitated in mass terms after 1 million years approaches the whole rock abundance found in the Osamu Utsumi mine. For example, with 15% porosity and a solid density of 2 g cm^{-3}, the maximum value shown in Figure 13 corresponds to 8,600 ppm (0.86%).

In the above respects the model is consistent with the observed occurrence of uranium in the mine. Further, the results suggest a local equilibrium approach may be adequate to describe steady-state conditions at the redox front. More accurate modelling is difficult at present owing to uncertainties regarding the effect of an oscillating water table on nodule dissolution and recrystallisation. Progress in this area will depend, therefore, on the incorporation of U-series data providing a framework for the permissible timescale of geochemical events.

4.2.5. Concluding discussion

A substantial amount of geochemical and hydrologic data has now been gathered on uranium behaviour at the Osamu Utsumi mine. The original intention that the site should provide a simple analogue for redox front reactions has not been realised, largely owing to the widespread occurrence of uranium in oxidised rock and the complexity of the hydrologic regime. Nevertheless, experimental and subsequent theoretical studies have elucidated the key processes governing uranium migration and tentative models for site evolution have been proposed.

The usefulness of conventional thermodynamic simulations in reproducing the main features of the site reflect observations that the bulk (>90%) of uranium transport occurs in true solution (Bruno *et al.*, this report series; Rep. 11). They also suggest that an equilibrium approach, used judiciously, is a valid approximation, given the relative rates of transport and mineral dissolution/precipitation reactions. For example, in this work the uptake of uranium by iron oxides was modelled as an equilibrium surface complexation reaction. This is based on evidence that dissolution rates for primary pitchblende are very slow compared to the oxidation of pyrite (Posey-Dowty *et al.*, 1987), thereby providing justification for a model that assumes leached uranium encounters an oxidised region where "$Fe(OH)_3$" has already formed. Even here, however, ageing

effects leading to irreversible fixation have not been addressed. Thus, in all cases, a kinetic approach is preferable provided adequate data can be found.

Although redox processes are obviously important at the Osamu Utsumi mine, reduction of U(VI) to U(IV) is clearly not the sole means through which retention of uranium occurs. Within both the laterite zone and the oxidised region above the front (Fig. 10), oxidative fixation of U(VI) complexes by iron oxyhydroxides dominates and, volumetrically, may constitute the major sink for uranium in the mine. These findings confirm the important role played by iron oxides in scavenging mobilised uranium as noted at other analogue sites around the world (Duerden, 1990; Read *et al.*, 1990). The need for rigorous predictive models which account quantitatively for uptake of actinides by oxide surfaces is evident.

At the redox front itself, localised remobilisation of uranium is occurring where oxidising waters are brought into contact with strongly reducing bedrock. This has resulted in dissolution and re-precipitation of pitchblende nodules in narrow mineralised zones. Attempts to model this situation using a directly coupled chemical transport model produce results which are in reasonable agreement with those derived from U-series isotope data and with the observed distribution of uranium at the front. Further work is required to incorporate the U-decay series studies within the modelling approach.

Whereas the redox front at 42 m depth considered above appears to have been immobile for at least one million years, "the weathering front" at 33 m has propagated downwards by about 50 cm during this period (MacKenzie *et al.*, this report series; Rep. 7). Although characterisation of the upper front is difficult owing to uncertainties regarding groundwater flow directions and the influence of mining, the two models agree in important respects. Uraninite precipitation is predicted to occur in very narrow zones within the reduced rock, consistent with localised pitchblende nodule formation.

4.3. Overview

It should be emphasised that the modelling studies described in the previous sections were carried out before the integrated conceptual model of the redox front described in Chapter 2 had been developed. The studies should, however, provide an interesting test of how well the modellers could carry out "blind" modelling of the redox front.

The Harwell model provides a reasonable description of some of the main aspects of the redox front, e.g. build-up of uranium concentration on the reduced side of the front, and reasonable concentrations of some dissolved species on both sides of the front. As

noted, however, the predicted pH was rather far from field measurements and the explanation invoked (i.e. contamination) is not supported by detailed analysis of the water chemistry (Nordstrom *et al.*, this report series; Reps. 6 and 14). Additionally, uraninite was predicted to precipitate whereas only pitchblende is found at Osamu Utsumi. The Harwell model also indicates complete removal of uranium in the oxidised zone, which is not consistent with observations. The Atkins model predicts uranium in the upper zone by considering incorporation of uranium sorption onto iron oxides. Although, in "static" calculations, such a mechanism could produce uranium concentrations in oxidised rock similar to those observed, reversible sorption should cause concentrations to show a net decrease going towards the infiltration point, which is the opposite of the trend observed.

Both models predict relatively low rates of front movement, which are compatible with field observations. Neither model, however, predicts the secondary pyrite formation which is characteristically associated with nodular pitchblende.

5. Kinetic modelling

P.C. Lichtner

5.1. Introduction

This chapter examines a kinetic approach to modelling the redox front, which contrasts with the equilibrium thermodynamics presented in the previous chapter.

The model used here is based on a Lagrangian representation of mass transport in a homogeneous porous medium. Mineral reactions are described through pseudo-kinetic rate expressions when more accurate rate laws are not available. Model calculations are carried out for pure advective transport in a single spatial dimension. The transport of uranium and weathering of the hydrothermally altered phonolite host-rock are considered together.

The computational procedure used is based on the quasi-stationary state approximation to transient mass transport equations. In this approximation the time evolution of a geochemical system in response to mass fluxes is represented by a sequence of stationary states. Each stationary state represents the fluid composition corresponding to a different state of alteration of the host-rock. The mathematical details can be found in Lichtner (1988). The first stationary state determines the initial sequence of mineral alteration zones. Subsequent stationary states account for precipitation and dissolution of minerals and the movement of mineral alteration zones with time.

A full kinetic treatment of mineral reaction rates is employed in the calculations presented here. This involves solving a system of nonlinear, ordinary differential equations. A kinetic description requires input data in the form of rate laws and their associated rate constants, surface areas of the reacting minerals and various other parameters describing, for example, the pH-dependence of the rate. Part of this investigation involved determination of the sensitivity of the results to the kinetic rate parameters. The model is described in more detail in Appendix 1.

5.2. Application to the Osamu Utsumi mine

5.2.1. Scope of calculation

In this section the reaction path model is applied to the Osamu Utsumi uranium mine. Of special interest is the occurrence of sharp redox fronts at which uranium is deposited. To compare predictions of a reaction path calculation with field data of borehole water analyses and mineralogy, it is necessary to know the travel time of groundwater from the point of recharge to the observation point. This necessitates knowledge of the length of the flow path and the fluid velocity along the streamline connecting the recharge point with the observation point. Furthermore it is necessary to know the host-rock composition along the flow path. Since it was clearly not feasible to determine this directly from field observations, some assumptions of continuity of mineralogy must be made if there is no evidence to the contrary. At the Osamu Utsumi mine the situation is additionally complicated because the flow regime has changed since construction of the open pit mine. As a consequence, direct comparisons of theoretical calculations with water analyses are difficult to interpret. For example, reducing conditions have not been measured in most of the deep boreholes which penetrate the reduced, hydrothermally altered phonolite host-rock. For this reason no attempt is made to quantitatively reproduce individual borehole water analyses. Rather, the focus is on a qualitative description of the weathered profile and redox front paragenesis.

The composition of a single packet of fluid is calculated as a function of travel time as the packet reacts with the hydrothermally altered phonolitic host-rock at the Osamu Utsumi mine. The host-rock minerals taken into account in the calculation are K-feldspar, kaolinite, muscovite in place of illite, fluorite and pyrite. Gibbsite, ferrihydrite and uraninite appear as secondary minerals. To simplify the calculations the host-rock is described as a homogeneous porous medium.

5.2.2. Input parameters

Thermodynamic data used in the calculations are taken from the EQ3/6 database DATA0R54, with the exception of muscovite (as discussed below) and uranium-bearing species, for which the data from Bruno and Puigdomenech (1989) are used. A kinetic description requires input data in the form of rate laws and their associated rate constants, surface areas of the reacting minerals and various other parameters. The rate coefficients used in the calculation are listed in Table VII. With the exception of K-feldspar, for which the rate law presented by Helgeson *et al.* (1984) was selected, for all other minerals a pseudo-kinetic rate law is used. For gibbsite, kaolinite and muscovite (muscovite is used as a substitute for illite), a rate coefficient 20 to 50 times that of K-feldspar is taken. Because the precipitation rate approaches the limiting local equilibrium value as the rate coefficient increases, it may be adjusted so that precipitation is close to equilibrium.

TABLE VII

Initial mineral volume fractions (ϕ_m^0), grain size (d_m) and kinetic rate coefficient (κ) used in the calculations. Grain size is based on average size along fractures (Waber *et al.*, this report series; Rep. 2).

Mineral		d_m	κ(moles $cm^{-3}sec^{-1}$)
pyrite	0.02	2 mm	1.5×10^{-14}
ferrihydrite	0.0	~50μ	1.5×10^{-14}
K-feldspar	0.6	1 cm	1.14×10^{-15}
muscovite	0.15	20μ	$2. \times 10^{-14}$
kaolinite	0.15	<2μ	$5. \times 10^{-14}$
gibbsite	0.0	-	$5. \times 10^{-14}$
fluorite	0.002	3 mm	$5. \times 10^{-15}$
chalcedony	0.0	-	1.6×10^{-17}
uraninite	0.0	-	$1. \times 10^{-17}$

The pyrite kinetic rate law is more problematic. Most experiments on the oxidation of pyrite have been concerned primarily with determining the rate far from equilibrium at low pH (≤ 4) (Nordstrom, 1982). Several authors have suggested that, for this case, Fe^{3+} acts as the major oxidant (Singer and Stumm, 1970; Wiersma and Rimstidt, 1982; McKibben and Barnes, 1986). More recent experiments suggest electro-chemical processes as a possible mechanism (Lowson, private communication). Very little is understood about the reaction mechanism at higher pH (≥ 4). Aqueous sulphur species with intermediate oxidation states, such as thiosulfate $S_2O_3^{2-}$, have been observed

(Goldhaber, 1983; Moses *et al.*, 1987). Pyrite is expected to react more rapidly than silicate minerals and therefore its rate may be mixed surface- and transport-controlled, taking place through a stagnant boundary layer surrounding the pyrite grains. This introduces an additional uncertainty into the rate expression.

The rate coefficient for uraninite is chosen to give a reasonable precipitation rate consistent with the modal abundance of uranium nodules found at the mine site. Uraninite is used in favour of U_3O_8 because of thermodynamic stability considerations, uraninite being the stable phase for a pH less than about 6 (see Fig. 21).

The fluorite rate coefficient is taken to be smaller than muscovite and kaolinite rate coefficients, but larger than K-feldspar. This results in a slow dissolution rate for fluorite, consistent with most water samples taken at the site, indicating undersaturation with respect to fluorite. Dobrovolsky and Lyalko (1983) have experimentally investigated fluorite kinetics and found it to be mixed surface- and transport-controlled at 25°C.

The water analysis from borehole F5, the deepest well drilled at the mine site, is used to constrain the initial fluid composition of the packet and the equilibrium constant for the muscovite (illite) hydrolysis reaction. Its composition is given in Table VIII along with initial and final fluid packet compositions for the reaction path calculation discussed below. Borehole F5 water is undersaturated with respect to K-feldspar, kaolinite and muscovite and in approximate equilibrium with fluorite and barite (not considered in the reaction path calculation). It is supersaturated with respect to chalcedony. In order for the silica concentration predicted by the reaction path calculation to become equal to or exceed the silica concentration measured in borehole F5, it is necessary to alter the log K of muscovite to move the K-feldspar-muscovite-kaolinite triple point to a higher silica value. A log K of 13.9 was chosen compared to the value of 14.56 in the EQ3/6 database DATA0R54. This also has the effect of lowering the final equilibrium potassium ion concentration of the reaction path, bringing it into better agreement with the borehole F5 value (see Fig. 24 below). With the original value of the muscovite equilibrium constant the potassium concentration was too high and the silica concentration too low. In any case the results are clearly very sensitive to the muscovite log K. This is true for other minerals as well, particularly kaolinite.

The results of three calculations are presented, involving the reaction of a single packet of fluid with the hydrothermally altered phonolite host-rock. The first example considers weathering of the host-rock in the absence of pyrite. The second and third examples combine weathering with the oxidation of pyrite and uraninite deposition. In the first two examples the inlet fluid is represented by rainwater infiltrating through a soil zone with the composition given in Table VIII. The sodium ion is inert in the path

TABLE VIII

Initial and final fluid compositions for a packet of fluid reacting with the hydrothermally altered phonolitic host-rock at the Osamu Utsumi uranium mine and the water analysis from borehole F5.

	Initial	Final	F5
pH	4.3	6.16	5.99/6.19*
Eh (V)	0.96	-0.11	0.462
Alkalinity**	0.19	8.54	23.5
Element		Concentration mg/l	
Ca	0.2	6.4	7.88
Mg	–	–	0.46
Sr	–	–	0.2
Ba	–	–	0.12
Na	0.63	0.63	0.63
K	0.39	16.06	11.8
Fe(II)	0.	1.38	6.13
Fe(III)	0.	0.	6.27
Al	0.	0.12	0.183
Mn	–	–	0.13
Zn	–	–	2.17
SO_4	1.92	15.17	28.0
F	0.	5.71	6.0
Cl	2.0	1.96	<2
Br	–	–	<0.05
SiO_2	0.06	38.02	34.0
U	0.00237	4.18×10^{-8}	–

*(field/lab) **mg/l HCO_3^-

calculation, its source determined by its concentration in rainwater (or soil water). A value equal to the borehole F5 analysis is taken. The chloride ion concentration is calculated by charge balance assuming values for the other species given in Table VIII, with an assumed pH of 4.3, a log P_{CO_2} of -2 and equilibrium with atmospheric oxygen. It is presumed that the infiltrating rainwater attains a total uranium concentration of 10^{-8} moles/litre near the surface. In the third example the inlet fluid is taken in equilibrium with the oxidised host-rock at a pH of 6.5.

5.2.3. Numerical results

In the absence of pyrite, weathering of the hydrothermally altered phonolite rock results in the rates of reaction of the packet of fluid with the host-rock as shown in Figure 16 (plotted as a function of the logarithm of the travel time). Initially K-feldspar, muscovite and kaolinite dissolve. Gibbsite begins to precipitate further down-gradient, followed almost immediately by a change in the sign of the kaolinite reaction rate resulting in the formation of secondary kaolinite. Muscovite and K-feldspar continue to dissolve along the length of the column. As equilibrium is approached, the rates of muscovite and kaolinite are reversed, with muscovite precipitating and kaolinite dissolving while K-feldspar continues to dissolve. These results are consistent with field observations of formation of a lateritic cover at the top of the weathered column followed by a saprolite zone consisting mainly of secondary kaolinite; secondary illite has also been observed (Waber *et al.*, this report series; Rep. 2). To obtain the development of the weathered profile with time, it would be necessary to integrate the effects of additional packets of fluid.

The calculated pH is shown in Figure 17. It increases steadily from its initial value of 4.3, becoming constant through the gibbsite-kaolinite zone (buffered by the transformation of kaolinite into gibbsite). It then increases sharply to a value of approximately 7, as the fluid comes into equilibrium with the hydrothermally altered phonolite.

Including pyrite in the set of primary minerals leads to the reaction rates shown in Figure 18 with the formation of a redox front marked, on this scale, by the disappearance of ferrihydrite and the right-angle bend in the pyrite oxidation rate as it plummets towards zero. These latter reactions divide the host-rock into oxidised and reduced regions. The initial part of the reaction path is similar to the first example with dissolution of the silicate minerals followed by the precipitation of gibbsite and kaolinite. A sharp spike occurs in the kaolinite precipitation rate at the redox front, indicating the coupling between redox and silicate hydrolysis reactions. This could explain the presence of a kaolinite-enriched zone formed between the oxidised and reduced rock observed at some of the redox fronts found near the surface of the mine (Waber *et al.*, this report series; Rep. 2).

A close-up view of the redox front is shown in Figure 19, where the reaction rates of ferrihydrite, uraninite and pyrite are shown as a function of the distance travelled by the packet in millimetres, assuming a Darcy flow velocity of 1 m yr^{-1}. As can be seen from the figure, the redox front actually consists of several closely spaced fronts over a distance

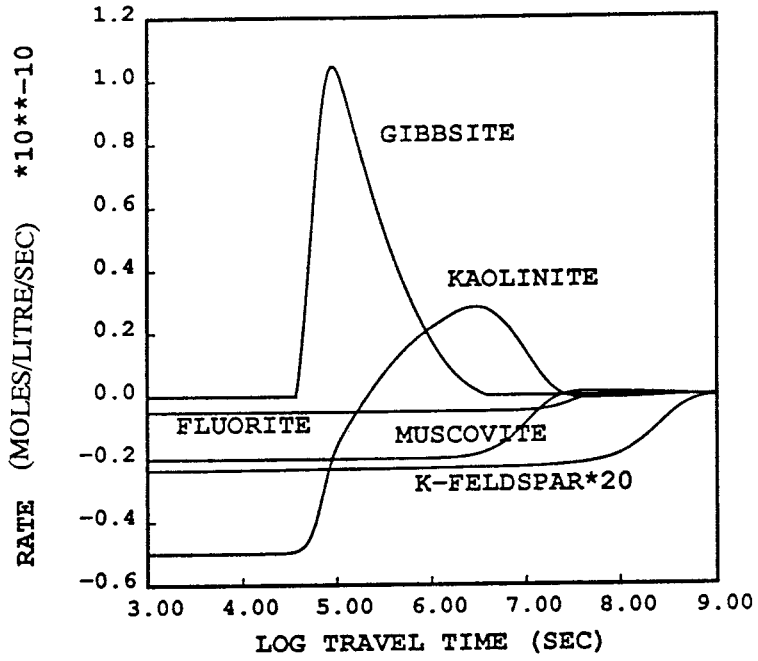

Figure 16. Weathering of hydrothermally altered phonolite rock by infiltrating rainwater in the absence of pyrite. Reaction rates of the indicated minerals are plotted as a function of the logarithm of the travel time in seconds for a packet of fluid moving with constant velocity through a homogeneous porous column of rock. The initial composition of the packet is given in Table VIII.

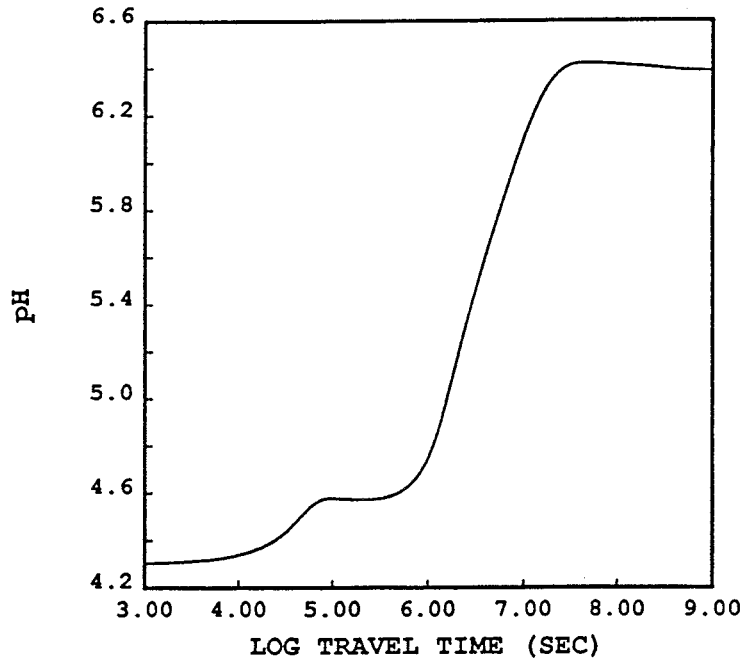

Figure 17. The pH plotted as a function of the logarithm of the travel time for a packet of fluid with the same conditions as in Figure 16.

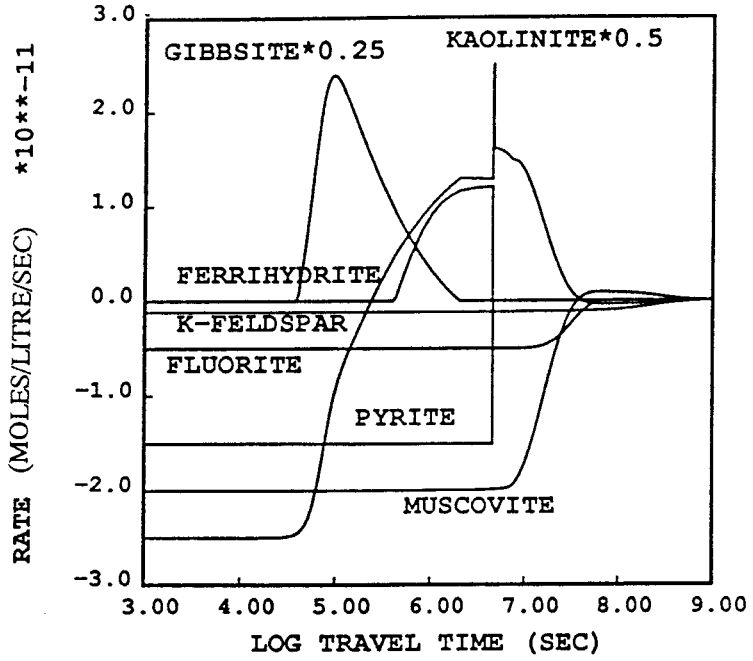

Figure 18. Weathering of hydrothermally altered phonolite rock including the oxidation of pyrite and uranium deposition with the same initial conditions as in Figure 16. Reaction rates of the indicated minerals are plotted as a function of the logarithm of the travel time in seconds for a packet of fluid moving with constant velocity. A sharp change in redox state of the packet occurs where the ferrihydrite and pyrite rates rapidly approach zero. At the redox front uraninite is deposited as shown in detail in Figure 19.

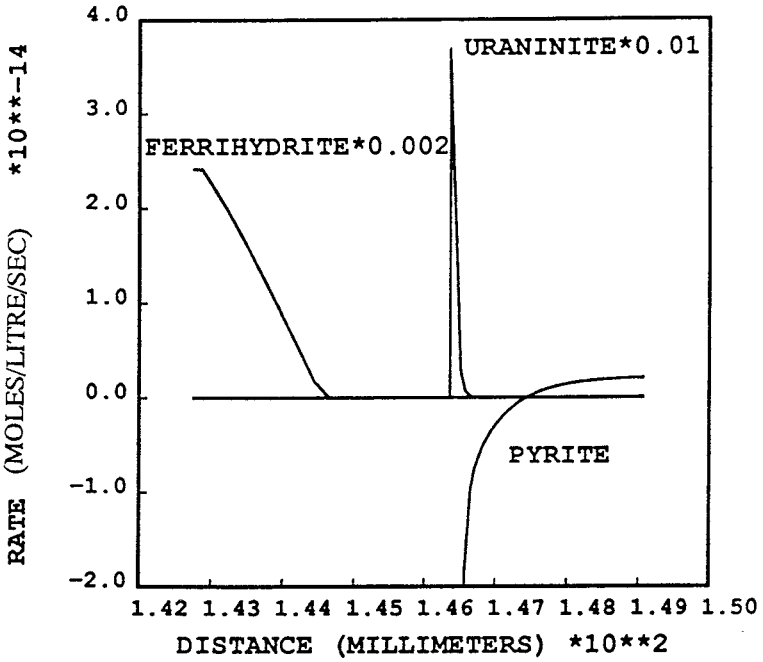

Figure 19. A close-up view of the redox front showing the reaction rates of pyrite, ferrihydrite and uraninite plotted as a function of distance. A Darcy flow velocity of 1 m yr^{-1} is assumed to convert travel time to distance. The placement of the uraninite zone and its narrow width are consistent with field observations at the Osamu Utsumi mine.

of several millimetres. The zone of uraninite precipitation is extremely narrow, so narrow in fact that it calls into question the neglect of diffusive transport in the calculation (see discussion). A narrow gap occurs between the ferrihydrite and uraninite zones with pyrite present along the entire flow path. According to the figure the pyrite rate drops rapidly within the uraninite zone as the uraninite precipitation rate drops exponentially to zero and begins to precipitate further downstream. These results, and the placement of the uraninite zone downstream from ferrihydrite precipitation, are consistent with field observations at the Osamu Utsumi mine. There, pitchblende nodules are observed to form, surrounding dissolving pyrite grains which lie on the reduced side of the iron oxide zone.

Precipitation of pyrite is shown in Figure 20. Formation of secondary pyrite has been observed in some of the uranium nodules at the Osamu Utsumi mine; presumably bacteria are necessary to catalyse the reaction.

As a summary of these results for the reaction path of the fluid packet, the data are plotted on a pe-pH activity diagram shown in Figure 21. As is clear from the figure, the spatial relation of the ferrihydrite and uraninite zones results as the reaction path crosses the stability field of uraninite in the Fe^{2+} aqueous window located on the reduced side of the ferrihydrite zone. This behaviour does not appear possible in a local equilibrium description which is restricted to the coexistence line of ferrihydrite and pyrite in the absence of diffusion (Lichtner, 1990). Note that U_3O_8 forms only at a higher pH or more concentrated uranium solutions which moves the stability line for U_3O_8 upwards relative to the uraninite stability line.

The pe is shown in Figure 22 as a function of the logarithm of the fluid packet travel time. It remains relatively constant and then drops sharply across the redox front. It then remains constant for a brief period and drops again as secondary pyrite is formed.

The pH gradually increases from its inlet value of 4.3 to approximately 4.5 and then decreases slightly as pyrite continues to dissolve as shown in Figure 23. A slight jump in pH occurs at the redox front, after which the pH sharply increases until equilibrium is reached with the hydrothermally altered phonolite host-rock. The pH is slightly less than its value in the absence of pyrite dissolution, as is evident by comparison with Figure 17.

In Figure 24 the reaction path is plotted on an activity diagram as a function of the activity of K^+ divided by the activity of H^+ versus the activity of SiO_2. Also shown is the borehole F5 analysis. The dashed muscovite field corresponds to a log K of 13.9 used in the calculation, whereas the solid line corresponds to the original log K in the EQ3/6 database. The silica concentration initially increases and then approximately follows the quartz saturation line as kaolinite precipitates. The potassium to hydrogen ratio steadily

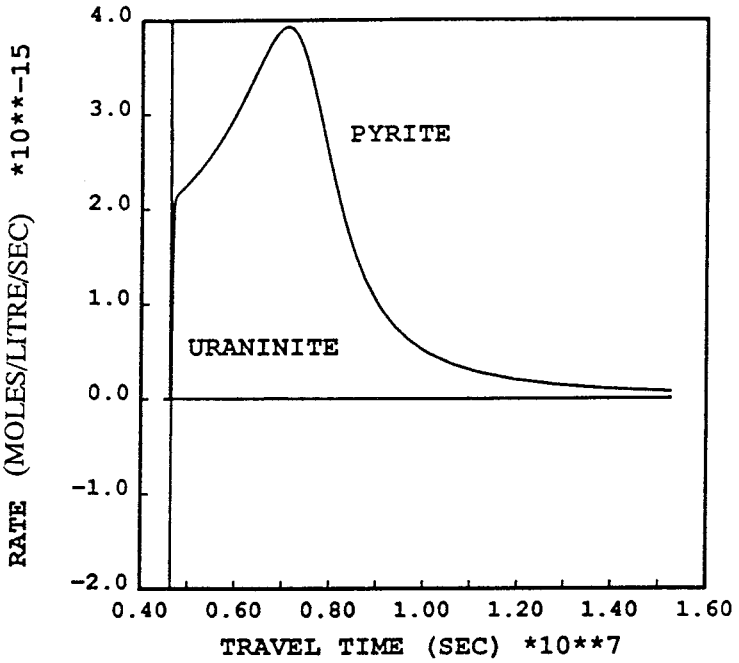

Figure 20. Formation of secondary pyrite following the deposition of uraninite (vertical solid lines) plotted as a function of travel time of a packet of fluid.

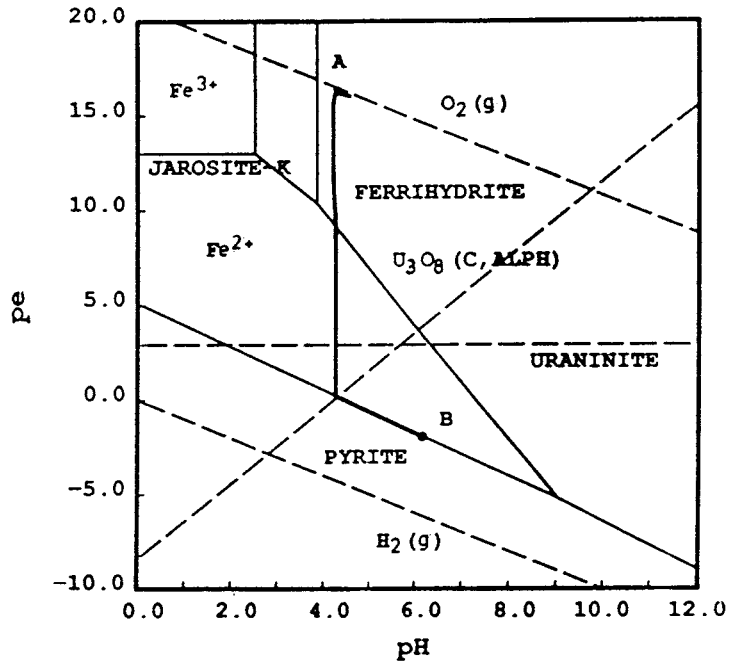

Figure 21. Activity diagram of pe versus pH showing the reaction path (solid curve) of a fluid packet reacting with pyrite-bearing hydrothermally altered phonolite host-rock. Stability lines for uraninite and U_3O_8 are shown as dashed lines.

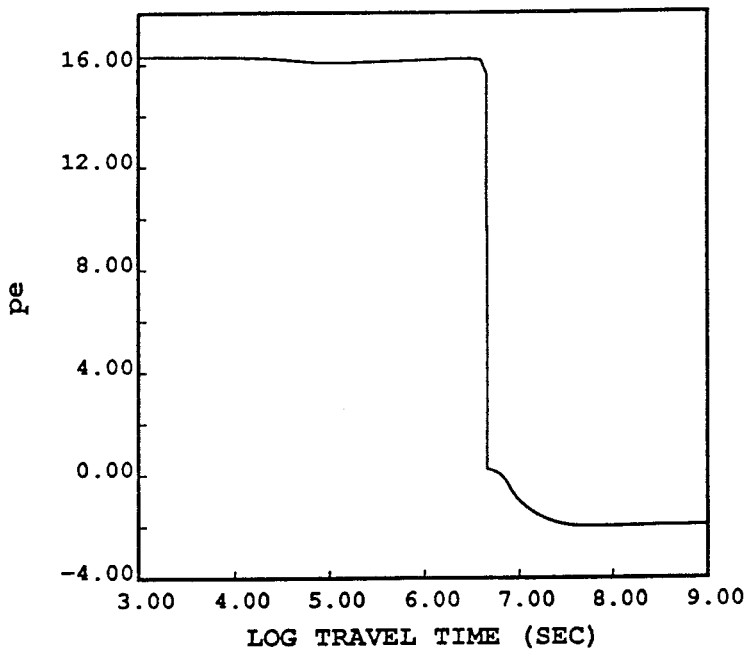

Figure 22. The pe plotted as a function of travel time of a packet of fluid. A sharp drop in the pe occurs at the redox front.

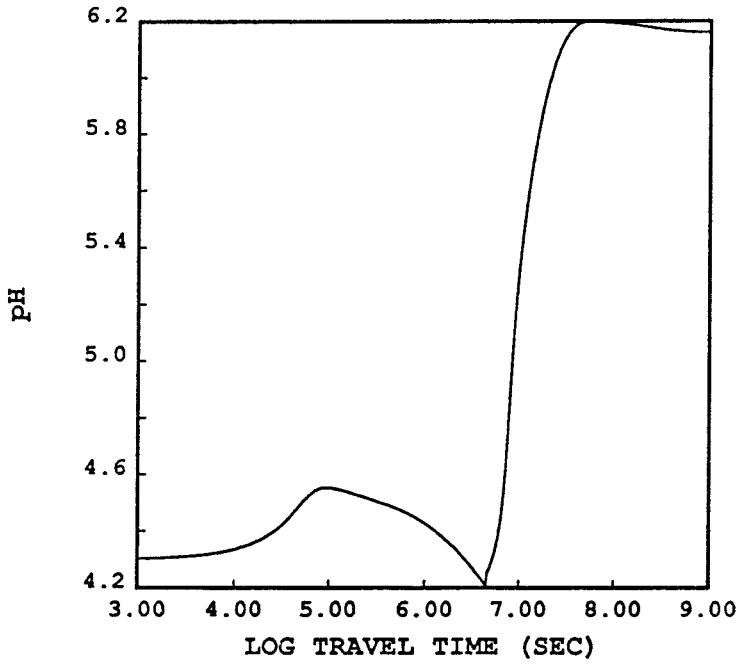

Figure 23. The pH plotted as a function of travel time of a packet of fluid. The decrease in pH results from the dissolution of pyrite. The pH rapidly increases as equilibrium is reached with the host -rock.

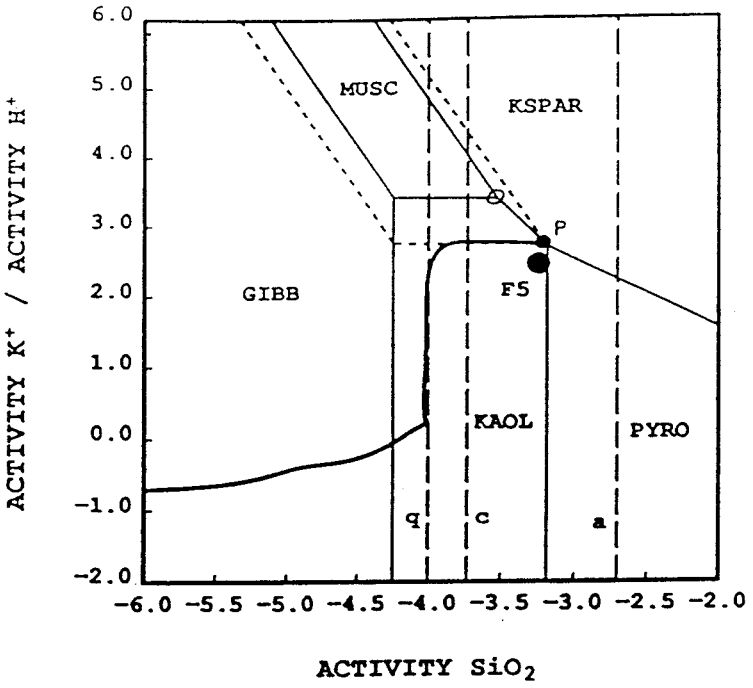

Figure 24. Reaction path (solid curve) plotted on an activity diagram in the variables K^+/H^+ versus SiO_2. The long-dashed vertical lines refer to the saturation lines for quartz (q), chalcedony (c) and amorphous silica (a). The field for muscovite used in the calculation corresponds to the dashed boundary. The F5 borehole analysis is shown as a solid dot. The point labelled P denotes the final equilibrium state of the reaction path.

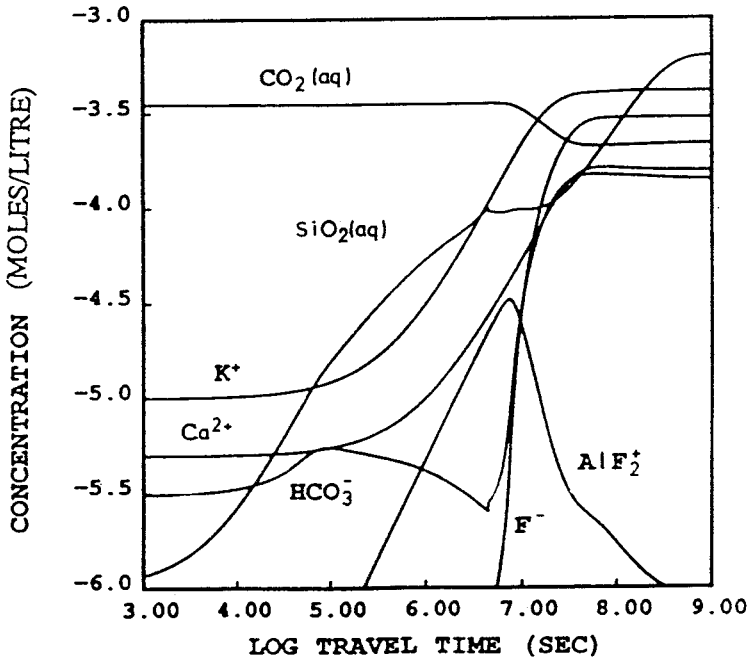

Figure 25. Log of the concentration of aqueous species K^+, Ca^{2+}, SiO_2, HCO_3^-, $CO_{2(aq)}$, F^- and AlF_2^+ plotted as a function of the log of the fluid packet travel time.

increases along the path. Equilibrium with respect to the minerals kaolinite and muscovite is reached first, followed by K-feldspar as the path moves along the muscovite-kaolinite boundary.

Selected aqueous species concentrations are shown in Figures 25–29. The iron, sulphur and uranium species are sensitive to the redox state and pH, whereas the aluminum and carbon species are sensitive to the increase in pH as the fluid comes to equilibrium with the altered phonolite rock.

In Figure 25 the concentrations of aqueous species K^+, Ca^{2+}, SiO_2, HCO_3^-, $CO_{2(aq)}$, F^- and AlF_2^+ are plotted as a function of the packet travel time.

The aluminum speciation is shown in Figure 26. The dominant aqueous aluminum species becomes AlF_2^+ as the concentration of fluoride increases with travel time, resulting from fluorite dissolution (see Fig. 25).

The speciation of iron is shown in Figure 27. The major change in iron chemistry across the redox front is to reduce ferric to ferrous iron. However, in the region where secondary pyrite forms, the opposite transformation apparently takes place. The amount of ferrous iron oxidised to ferric iron is too small to be noticeable in the figure.

The aqueous sulphur chemistry is shown in Figure 28. The dominant sulphur species is sulphate which gradually increases as pyrite dissolves until the redox front is reached, after which it remains essentially constant. There is a sharp increase in the concentrations of H_2S and HS^- at the redox front. Their concentrations rapidly decrease as secondary pyrite is formed.

The uranium speciation is shown in Figure 29. The predominant uranium valence state changes from VI on the oxidised side of the redox front in the form of UO_2^{2+} to IV and V on the reduced side in the form of $U(OH)_4$ and UO_2^+ respectively. On the reduced side of the redox front the uranium concentration is depleted by four orders of magnitude resulting from uraninite precipitation.

As pyrite begins to completely dissolve along the uppermost part of the flow path, oxidising water can penetrate deeper into the host-rock. Therefore as the system evolves in time and the redox front is displaced further along the flow path, the pH at the front will tend to increase. In the extreme case that the infiltrating fluid has sufficient time to achieve equilibrium with the oxidised portion of the host-rock, the pH at the redox front will have increased to near its maximum possible value. To explore the effect of pH on the redox front, the final example assumes the inlet fluid is in equilibrium with the oxidised host-rock consisting of the minerals K-feldspar, muscovite and ferrihydrite at a pH of 6.5. The mineral reaction rates are shown in Figure 30. In this case gibbsite does not form as an alteration product. The same sequence of reactions occurs at the redox

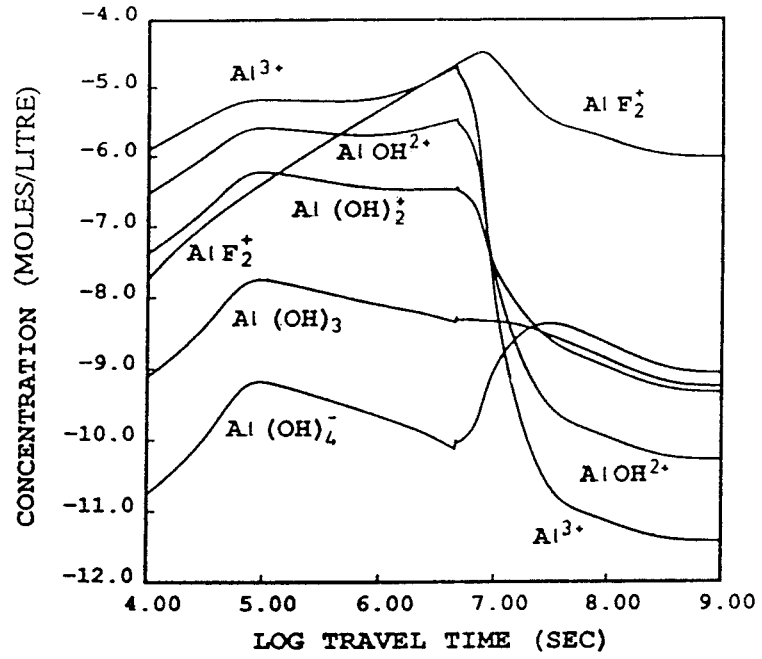

Figure 26. Log of the concentration of aqueous aluminum species including selected fluoride complexes plotted as a function of the log of the fluid packet travel time.

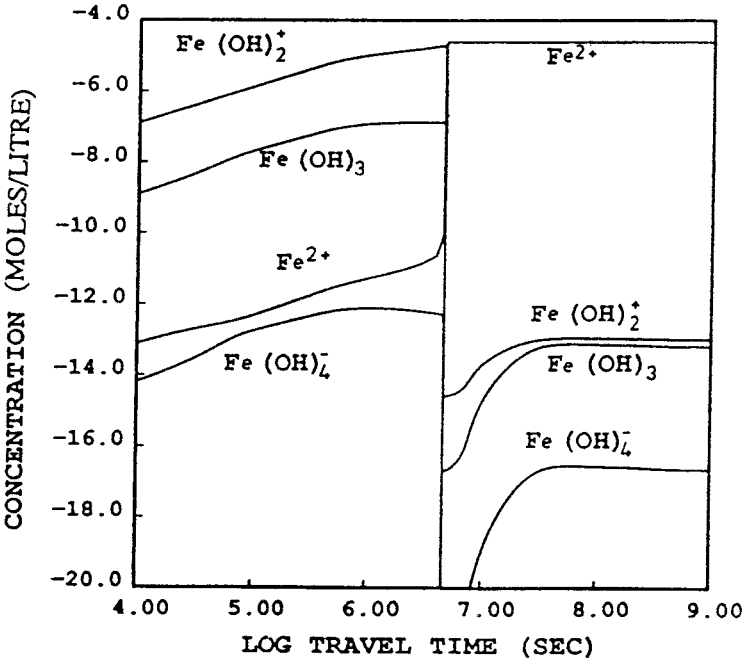

Figure 27. Log of the concentration of aqueous iron species plotted as a function of the log of the fluid packet travel time.

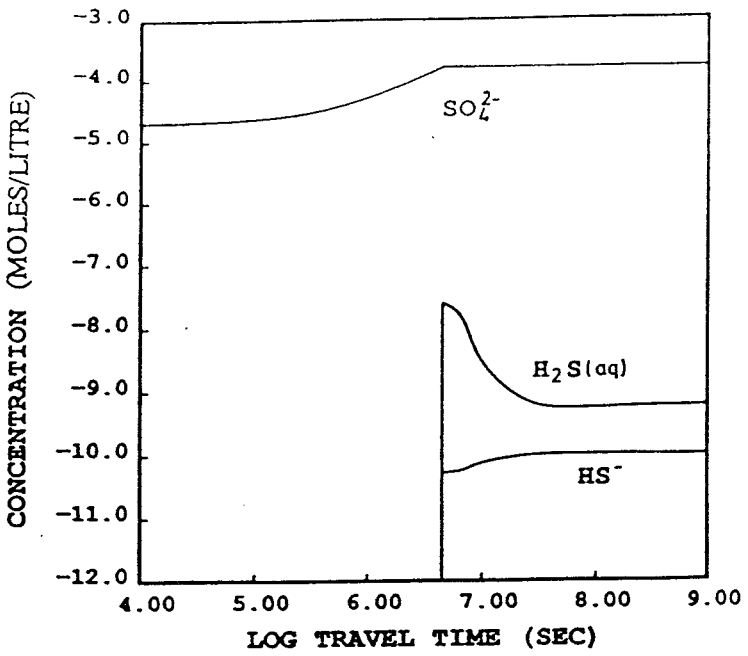

Figure 28. Log of the concentration of aqueous sulphur species plotted as a function of the log of the fluid packet travel time.

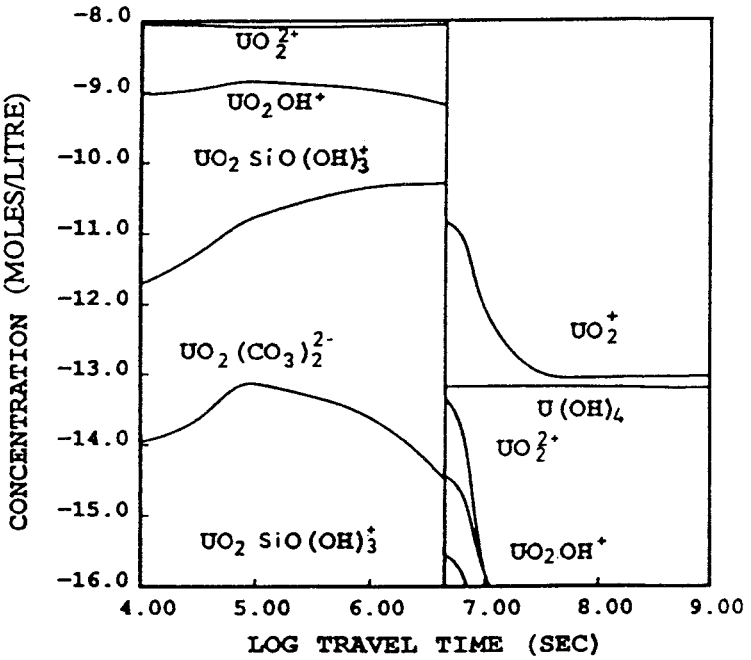

Figure 29. Log of the concentration of aqueous uranium species plotted as a function of the log of the fluid packet travel time.

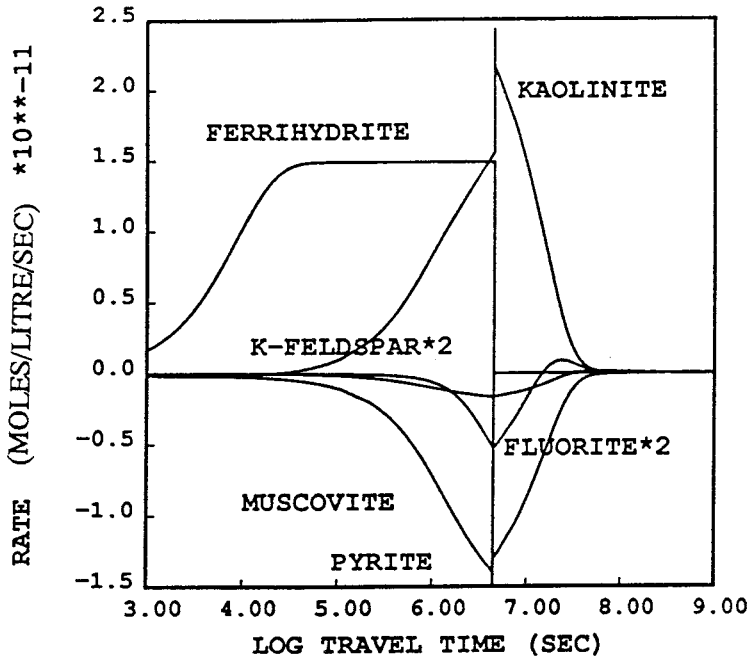

Figure 30. Reaction rates plotted as a function of travel time for an inlet fluid with pH 6.5 in equilibrium with the oxidised, altered phonolite host-rock.

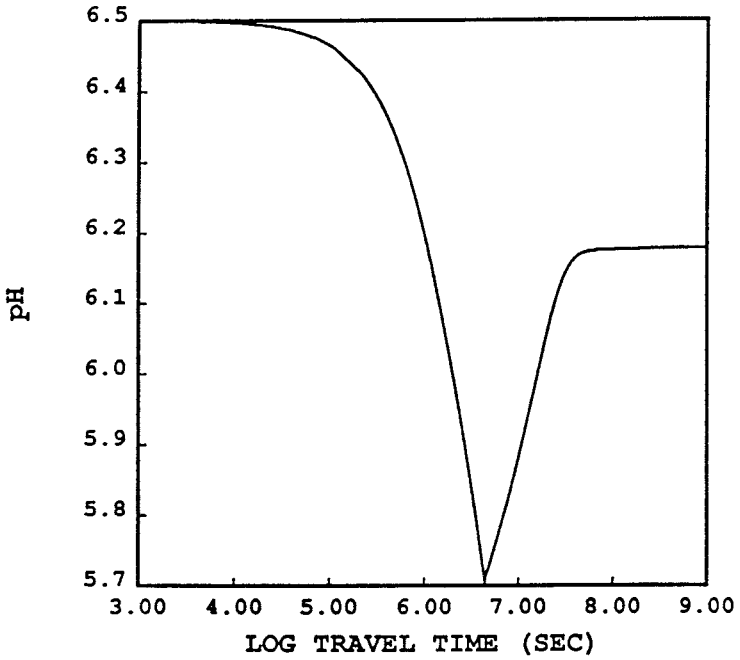

Figure 31. The pH plotted as a function of travel time for the same conditions as in Figure 30.

front with precipitation of uraninite following ferrihydrite precipitation. The pH is shown in Figure 31 as a function of the logarithm of the travel time.

5.3. Discussion

The results obtained above for the reaction path of a single packet of fluid seem to be able to qualitatively describe the mineralisation observed at the Osamu Utsumi mine. From the analysis of a single packet of fluid, however, it is not possible to deduce the time evolution of the various reaction zones. Nevertheless it is possible to speculate on the migration of the uraninite precipitation zone. One possible mechanism consistent with the results obtained above is a "hopping" behaviour rather than a continuous movement. This may be argued as follows by considering the behaviour of the second reaction path. This path differs from the first path in that pyrite will have completely dissolved up to the redox front. The next packet of fluid would then first encounter uraninite before pyrite. The fluid would still be oxidising. Under these circumstances uraninite would be unstable and would dissolve. Because the uraninite zone is too narrow for the fluid packet to come to equilibrium within the zone, the entire uraninite zone would dissolve. Eventually, as dissolution of pyrite occurred, the packet would again cross the uraninite stability field precipitating uraninite further down-gradient and come to equilibrium with pyrite. In this way the uraninite nodules would hop from one location to the next.

Some field evidence exists for such a hopping mechanism. First, completely dissolved uraninite nodules characterised by bleached areas in the oxidised portion of the hydrothermally altered phonolite have been observed, consistent with a hopping mechanism. Second, partially dissolved uraninite nodules cut by a sharp redox front have rarely been observed.

For a Darcy flow velocity of 1 m yr^{-1}, the width of the uraninite zone is in the order of 0.02 mm according to Figure 19. However, according to field observations, the nodules are in the order of several centimetres. Thus the model calculations underestimate the width of the uraninite precipitation zone by several orders of magnitude compared to the width of typical nodules observed in the field. There are two possible explanations for this discrepancy. One explanation is that, with increasing time, the nodules increase in size as they dissolve at the upstream side and reprecipitate further downstream. Such behaviour corresponds to the usual description for the propagation of a reaction zone.

This would imply, however, that the nodules continuously advance in time, which is not corroborated by observation.

An alterative explanation is that diffusive transport is an important mechanism in determining the size of the nodules and needs to be included in the calculation. Assuming a Darcy flow velocity of 0.1 m yr^{-1}, a porosity of 10% and a diffusion coefficient of 10^{-5} $cm^2\,sec^{-1}$, the characteristic diffusion length λ is in the order of

$$\lambda = \frac{\phi D}{u} \sim 3\text{cm} \qquad (1)$$

much larger than the calculated width of the uraninite zone for pure advective transport. The roughly oblong growth of the nodules can therefore be explained by a combination of advection and diffusion with diffusion smearing out the needle-like precipitation obtained in the pure advective case. Thus it would appear that diffusion is an important mechanism in their formation.

Several comments are worth making about the final equilibrated reaction path and its comparison with the water analysis taken from borehole F5 (presented in Table VIII).

- One obvious difference between the two waters is the redox potential. F5 is oxidising, whereas the reaction path water is in equilibrium with pyrite and hence reducing. The major cation K^+ is well-accounted for in the reaction path by dissolution of muscovite (illite) and K-feldspar.
- Sulphur concentration is due entirely to the dissolution of pyrite in the reaction path calculation. It is a factor two lower than the measured borehole F5 concentration.
- The calculated iron concentration is several orders of magnitude lower than the measured values.
- Fluorite and calcium concentrations are in good agreement with the measured values, with the calculated calcium concentration slightly less than the measured value. As the calculated concentration values for these species results from dissolution of fluorite, the good agreement would suggest that this is also the case at borehole F5. It should also be noted that the calculated equilibrium values are approximately independent of the fluorite kinetic rate law. This follows by noting that the rate of change with travel time of the calcium and fluoride concentrations satisfy the differential equations

$$\rho \frac{dm_{Ca}}{dt'} = -I_{CaF_2} \qquad (2)$$

and

$$\rho \frac{dm_F}{dt'} = -2I_{CaF_2} \tag{3}$$

where aqueous complexing has been neglected. Multiplying the first equation by two and subtracting the second yields the result

$$\frac{d}{dt'}(2m_{Ca} - m_F) = 0 \tag{4}$$

Thus the quantity in brackets is conserved along the flow path and it follows that

$$2m_{Ca} - m_F = 2m^0_{Ca} - m^0_F \tag{5}$$

where m^0_{Ca} and m^0_F denote the initial concentrations of calcium and fluoride ions, respectively. From this result it is possible to calculate the final concentrations of calcium and fluoride when the fluid packet reaches equilibrium with fluorite *without* any knowledge of the kinetic rate law for fluorite dissolution. Note that this statement is true regardless of how the fluorite grain size, surface area or abundance may change along the flow path. Combining the above conservation relation with the mass action equation for fluorite,

$$\gamma_{Ca} m_{Ca} (\gamma_F m_F)^2 = K_{CaF_2} \tag{6}$$

provides two equations for the final equilibrium concentrations. For an initial value of $m^0_{Ca} = 0.2$ mg l^{-1} and zero for m^0_F , the solution yields $m_{Ca} = 6.18$ and $m_F = 5.67$ mg l^{-1}, taking into account activity coefficient corrections with $\gamma_{Ca} = 0.86$ and $\gamma_F = 0.96$, in close agreement with the borehole F5 water analysis.

- Although an attempt was made to account for the concentration of zinc in solution through dissolution of sphalerite, this failed because sphalerite precipitated at the redox front, resulting in very low concentrations of Zn^{2+}. In any case sphalerite has not been observed in the vicinity of the redox front and only minor amounts of hydrothermally formed sphalerite are found at the mine site (Waber *et al.*, this report series; Rep. 2). Secondary sphalerite has not been observed to date.

- The observed formation of secondary pyrite appears to be accounted for by the model calculations. The reaction mechanism is apparently

$$2Fe(OH)_3 + 2H_2S + 2H^+ \rightarrow FeS_2 + Fe^{2+} + 6H_2O \qquad (7)$$

in which iron is reduced from iron III to iron II, and sulphur is oxidised from oxidation state -II to -I. Secondary pyrite formed only in the presence of silicate minerals, with or without uranium being present. It is found to occur associated with some of the uranium nodules at the Osamu Utsumi mine. Furthermore it occurs in some of the nodules but not in all. Secondary pyrite precipitation is a common occurrence in other roll-front type uranium deposits (Granger and Warren, 1969).

- According to the model calculations, relict pyrite should exist in the region where ferrihydrite is deposited unless, by coincidence, the pyrite dissolution reaction has gone to completion. Relict pyrite in the oxidised zone has not been observed so far, but it could be difficult to observe since the pyrite grains would be coated with iron oxides.

Finally a few remarks are made regarding the sensitivity of the calculation on the mineral rate coefficients. Increasing the pyrite rate coefficient tends to move the redox front closer to the inlet. The redox front paragenesis of ferrihydrite precipitation followed by uraninite is not altered. Nor is increasing the rate coefficient expected to affect the rate of advance of the redox front, which should be controlled by the supply of oxygen to the system.

The detailed shape of the reaction path in activity space K^+/H^+ versus SiO_2 depends on the relative rates of muscovite, kaolinite and K-feldspar chosen. Nevertheless the K^+/H^+ ratio and the concentration of SiO_2 of the final equilibrium point of the path is fixed by the muscovite-kaolinite-K-feldspar triple point. The final equilibrium pH depends on the rate coefficients.

The width of the uraninite zone varies with the magnitude of the uraninite rate coefficient. As the rate coefficient increases, a minimum width corresponding to the local equilibrium limit is obtained.

5.4. Conclusions

The calculations presented above indicate that it is possible to understand in considerable detail field observations of the uranium roll-front deposit at the Osamu Utsumi mine. The location of a narrow uraninite precipitation zone on the reduced side of the redox front obtained from the calculations is consistent with field observations, as is formation of secondary pyrite in the vicinity of the uranium nodules and a razor-sharp iron oxide redox front. The calculated width of the nodules is narrower than observed in the field, indicating that diffusive transport is probably an important mechanism in their formation. Nevertheless the results obtained here are extremely promising for more detailed calculations.

Future extensions and improvements of the calculations presented here should include the following:

1) Time Evolution. The calculations presented here represent a single reaction path formed by the first packet of fluid. To obtain the time evolution of the various reaction zones it is necessary to consider additional reaction paths. Calculating the velocity of propagation of the various reaction fronts will provide an important test of the model, especially regarding the proposed mechanism for advancement in time of the uraninite zone. Results must be consistent with field estimates of erosion rates, the observed penetration depth of the redox front, and the extent of laterisation that has taken place.

2) Pyrite Dissolution Rate Law. Perhaps the most uncertain element in the model calculations is the pyrite rate law. Disequilibrium in the aqueous solution must be considered, including such sulphur intermediaries as thiosulphate. It may also be necessary to include other iron sulphides which could act as intermediaries to the formation of secondary pyrite.

3) Diffusive Transport. Diffusive transport should be included in the calculations to account for smearing out of the uraninite precipitation zone.

4) Replacement for Muscovite-Illite. When reliable data for illite are available it should replace muscovite currently being used in the model calculations.

6. Synthesis

6.1. Review of modelling results

In the preceding chapters a range of modelling approaches have been used to attempt to explain the formation and movement of the redox front and make testable predictions.

The simple mass balance approach described in Chapter 3 yields rates of movement of the redox front which are somewhat larger than expected from geomorphological evidence (Holmes *et al.*, this report series; Rep. 5) or natural series radionuclide profiles (MacKenzie *et al.*, this report series; Rep. 7). It is clear that the extrapolation of present-day conditions to periods in excess of 10^6 years is overly simplistic, while assumption of a single advective supply of dissolved oxygen in meteoric water ignores the effects of water table oscillations in this sub-tropical climate and other important oxidants which may be present in low pH waters (e.g. Fe(III), SO_4). The more sophisticated treatment of channelling within fissure networks provides a qualitative explanation for the observed fingering but does not provide front migration rates which are as slow as found in nature, possibly because of the simplicity of the chemical side of this model.

The two coupled transport/chemical equilibrium models described in Chapter 4 differed to a fair extent in their mechanistic description of redox front chemistry but both could simulate most of the major features of the redox front. Although both models included constraints set by "assumed" values of pe, pH, etc., there are clear divergences between the predicted values of some parameters and those observed in the field. A critical area here is clearly the pe and pH buffering reactions assumed, as these parameters are major determinants of overall chemistry. Neither model was capable of simulating the observed formation of secondary pyrite in association with pitchblende nodules.

In terms of describing the chemistry of the redox front, the kinetic model described in Chapter 5 appears to perform reasonably well. It should be noted, however, that this model is the result of several iterations of development and, due to the lack of appropriate kinetic data, contains a fair amount of best-fit or assumed values. This model does, however, simulate the observed formation of secondary pyrite. In its current form, it does not evaluate the rate of redox front movement.

It should be noted that standard geochemical modelling techniques, considering a much wider range of minerals than is possible in any of these coupled calculations, can explain most of the major element changes during groundwater evolution at the Osamu

Utsumi mine (Nordstrom *et al.*, this report series; Rep. 14). Modelling the trace element chemistry was more problematic (Bruno *et al.*, this report series; Rep. 11).

6.2. Additional input

The conceptual model of the redox front which formed the basis for the models discussed above included only the major mineralogy/water chemistry from field observations. Detailed analysis of trace element distributions and measurement of radioactive and stable isotopes yield further information which can be examined in the light of these models. Important features are:

1) The natural series radionuclide profiles which indicate that individual fronts move at different rates and that these range from $\approx$ 1-10 m/10^6 years to <1 m/10^6 years.

2) Various trace elements are highly enriched on both sides of the redox front – many of which are not expected to be particularly redox-active. A few elements are preferentially concentrated on either the oxidising or the reducing side of the front.

3) S-isotope analysis of pyrite shows distinct differences between the secondary pyrite and the primary pyrite (Waber *et al.*, this report series; Rep. 2), the former being much lighter, which is suggestive of biological reworking. The intimate association of secondary pyrite with nodular pitchblende would be consistent with the form of the latter being due to biological activity.

Further, in the analysis of microbiological observations around the redox front, a model was developed in which it was assumed that both the oxidation of pyrite in the oxidising zone and formation of secondary pyrite and pitchblende in the reducing zone were microbially mediated (West *et al.*, this report series; Rep. 10). In this model, it is assumed that disulphide oxidation initially goes as far as an intermediate S species in solution, which is oxidised further on the reducing side of the front associated with the reductive formation of the U mineralisation. Organic carbon could also be an important reductant in this system, but is not considered in any of the current models.

Points 1) and 2) together indicate that advective transport of solute over the redox front is so slow that diffusion is a major, if not dominant, transport mechanism. Although possibly influenced by the geometry of the fronts studied, this could indicate that the hydraulic conductivity through the redox front is lower than in the surrounding rock. This is not unreasonable given the porosity changes associated with the oxidation

reactions and is especially suggested in the cases where a thin clay layer is found at the redox front. Microbial growth in this area may also reduce conductivity by pore clogging or the presence of biofilms.

6.3. Realistic modelling of redox fronts

In previous repository performance assessments, redox front movement has been estimated on the basis of simple mass balance calculations and the chemistry involved represented by a single redox buffering reaction. The Poços de Caldas studies indicate that such an approach may well be conservative – overpredicting the movement of such fronts and underestimating the extent to which they may retard radionuclides. The models poorly predict Eh/pH conditions at the redox front, however, and, if this could be significant (e.g. in determining speciation of a key element), they should be used with caution.

Examination of the discrepancies between model predictions and observations in the field indicate areas in which such models could be improved:

1) Better representation of multi-electron redox processes – in particular of sulphur species.
2) Including consideration of co-precipitation and solid solution of relevant trace elements.
3) Explicit consideration of kinetics using independently measured parameters.
4) Direct consideration of microbial activity.
5) Consideration of the changes in porosity resulting from mineral alterations and the consequent effect on hydraulic properties.

7. Conclusions

The chemistry of redox fronts at Poços de Caldas is much more complex than initially apparent. Although the main processes of pyrite oxidation to form iron oxyhydroxide and pitchblende oxidation/reduction are relatively easy to simulate using a range of modelling techniques, these models do not predict the complexity observed at the redox front.

Very simple mass balance calculations overpredict the rate of redox front movement and it is clear that, in such a perturbed system, such calculations can only be used as very crude scoping exercises. Coupled chemical thermodynamic/transport models can predict some of the major alterations occurring over the redox front, but poorly represent the main pH/redox buffering reactions. Kinetic models can provide a more detailed simulation of the observed front, but, due to the amount of fitting involved, need to be tested at another location before any extrapolation beyond this site could really be justified.

Semi-quantitative modelling of the microbiological processes occurring around the redox front indicates that complex aqueous sulphur chemistry, which is not considered in the chemical models, could play an important role. As yet, the input data needed to model such complex sulphur behaviour by either equilibrium or kinetic approaches are not available, although, in principle, the models could treat such a case. Although not very accurate in detail, the models used would tend to be "conservative" in a safety assessment sense, by overpredicting the rate of redox front movement. Additionally, the models would not predict the strong concentration of a wide range of trace elements around the redox front – probably because of the current lack of data on co-precipitation/solid solution formation.

8. Acknowledgements

David Read is grateful to Nick Waber and Peter Lichtner of the University of Bern for their helpful advice during the course of this work. His thanks also go to Nick Harrison of the UK Department of the Environment (DOE). The financial support of the DOE is gratefully acknowledged. He wishes to point out that the results of this work may be used in the formulation of Government Policy but at this stage do not necessarily represent Government Policy.

The Harwell group was funded by U.K. Nirex Ltd. as part of their Safety Assessment Research Programme, and this support is gratefully acknowledged.

Peter Lichtner's paper benefitted greatly from discussions with Nick Waber, Ian McKinley, Kirk Nordstrom and Tjerk Peters. He especially wants to thank Nick Waber for his tremendous effort in helping to put it all together. He is also grateful to Helmut Horn for his help with the graphics.

9. References

Aagaard, P., and Helgeson, H.C., 1982. Thermodynamic and kinetic constraints on reaction rates among minerals and aqueous solutions. I. Theoretical considerations, *Amer. J. Sci.* 282, 237-285.

Abelin, H., Neretnieks, I., Tunbrant, S. and Moreno, L., 1985. Final Report of the Migration in a single fracture – Experimental results and evaluation. *Stripa Proj. Rep.* (85-03), OECD/NEA, SKB, Stockholm, Sweden.

Bolvede, P. and Christianson, R., 1987. SKB Forsmarksarbetena SFR. Vattenförande sprickor inom lagerområdet. *VIAK Int. Rep.*, Stockholm (in Swedish). Water bearing fractures in the repository area.

Bruno, J. and Puigdomenech, I., 1989. Validation of the SKBU1 uranium thermodynamic data base for its use in geochemical calculations with EQ3/6. In: Scientific Basis for Nuclear Waste Management, XII, *Mat. Res. Soc. Symp. Proc.*, 127, 887-896.

Cooper, R.S. and Liberman, D.A., 1970. Fixed-bed adsorption kinetics with pore diffusion control, *Ind. Eng. Chem. Fundam.*, 9, 4, 620.

Cross, J.E. and Ewart, F.T., 1990. HATCHES: A thermodynamic database and management system. *Radiochim Acta* (in press).

Davis, J.A. and Leckie, J.O., 1978. Surface ionisation and complexation at the oxide/water interface II. Surface properties of amorphous iron oxyhydroxide and adsorption of metal ions. *J. Colloid Interface Sci.*, 67, 90-107.

Dobrovolsky, E.V., and Lyalko, V.I., 1983. Dynamics of groundwater fluoride: a model for the effects of kinetic and infiltration factors, *Geochem. Inter.* 20, 68-81.

Duerden, P. (ed), 1990. Alligator Rivers Analogue Project – First Annual Report, *ANSTO*, Australia.

Economides, V., Dawes, A. and Read, D., 1989. Chemical modelling studies in support of HMIP probabilistic risk assessment. *DOE Tech. Rep.* (TR-WSA-25), London, U.K..

Goldhaber, M.B., 1983. Experimental study of metastable sulphur oxyanion formation during pyrite oxidation at pH 6-9 and 30°C. *Am. Jour. Sci.* 283, 160-171.

Granger, H.C. and Warren, C.G., 1969. Unstable sulphur compounds and the origin of roll-type uranium deposits, *Econ. Geol.* 64, 160-171.

Haworth, A., Sharland, S.M., Tasker, P.W. and Tweed, C.J., 1988. A guide to the coupled chemical equilibria and migration code CHEQMATE, *Harwell Lab. Rep.*, (NSS R113), Harwell, U.K..

Helgeson, H.C., Murphy, W.M. and Aagaard, P., 1984. Thermodynamic and kinetic constraints on reaction rates among minerals and aqueous solutions. II. Rate constants, effective surface area, and the hydrolysis of feldspar, *Geochim. Cosmochim. Acta*, 51, 3137-3153.

Hsi, C-K, D. and Langmuir, D., 1985. Adsorption of uranyl onto ferric oxyhydrates. Application of the surface complexation site – binding model. *Geochim. Cosmochim. Acta*, 49, 1931-1941.

KBS-3, 1983. Final storage of spent nuclear fuel – KBS-3. *SKBF/KBS Tech. Rep.*, Stockholm, Sweden. (5 volumes).

Kent, D.B., Tripathi, V.S., Ball, N.B. and Leckie, J.O., 1986. Surface complexation modelling of radionuclide adsorption in sub-surface environments. *Stanford Univ. Tech. Rep.* (294), Stanford, U.S.A..

Lasaga, A.C., 1984. Chemical kinetics of water-rock interactions, *J. Geophys. Res.* 89, 4009-4025.

Lei, W., 1984. Thorium mobilisation in a terrestrial environment. *Ph.D. Thesis*, New York University, N.Y. 414 pp.

Lemire, R.L., 1988. Effects of high ionic strength groundwaters on calculated equilibrium concentrations in the uranium-water system. *AECL Tech. Rep.* (AECL 9549), Pinawa, Canada.

Liew, S.K. and Read, D., 1988. Development of the CHEMTARD coupled process simulator for use in risk assessment. *UK DOE Tech. Rep.* (DOE/RW/88.051), London, U.K..

Lichtner, P.C., Helgeson, H.C., and Murphy, W.M., 1987. Lagrangian and Eulerian representations of metasomatic alteration of minerals. In: H.C. Helgeson (Editor), Proc. NATO Advanced Study Institute on Chemical Transport in Metasomatic Processes, *Reidel, Dordrecht*, Holland, 519-545.

Lichtner, P.C., 1988. The quasi-stationary state approximation to coupled mass transport and fluid-rock interaction in a porous medium, *Geochim. Cosmochim. Acta*, 52, 143-165.

Lichtner, P.C., 1990. In: H. Ganguly (Editor), Advances in Physical Geochemistry, The quasi-stationary state approximation to fluid/rock interaction: local equilibrium revisited. *Springer Verlag* (in press).

McKibben, M.A. and Barnes, H.L., 1986. Oxidation of pyrite in low temperature acidic solutions: rate laws and surface textures, *Geochim. Cosmochim. Acta*, 50, 1509-1520.

McKinley, I.G. and Bradbury, M., 1989. Near-field geochemistry of vitrified HLW in a sedimentary host rock. In: Scientific Basis for Nuclear Waste Management, XII, *Mat. Res. Soc. Symp. Proc.*, 127, 645-651.

Moses, C.O., Nordstrom, D.K., Herman, J.S. and Mills, A.L., 1987. Aqueous pyrite oxidation by dissolved oxygen and by ferric iron, *Geochim. Cosmochim. Acta*, 51, 1561-1571.

Murphy, W.M., Oelkers, E.H., and Lichtner, P.C., 1989. Surface reaction versus diffusion control of mineral dissolution and growth rates in geochemical processes, *Chem. Geol.* 78, 357-380.

Neretnieks, I., 1984. The impact of alpha radiolysis on the release of radionuclides from spent fuel in a geologic repository. In: Scientific Basis for Nuclear Waste Management, VII, *Mat. Res. Soc. Symp. Proc.*, 26, 1009-1022.

Nordstrom, D.K., 1982. In: L.R. Hossner, J.A. Kittrick and D.F. Fanning (Editors), Aqueous pyrite oxidation and the consequent formation of secondary iron minerals, in Acid Sulfate Weathering: Pedogeochemistry and Relationship to Manipulation of Soil Materials. *Soil Science Soc. Amer. Press*, Madison, 37-62.

Palmqvist, K. and Stanfors, R., 1987. The Kymmen power station TBM tunnel. Hydrogeological mapping and analysis. *SKB Tech. Rep.* (TR 87-26), Stockholm, Sweden.

Parkhurst, D.L., Thorstenson, D.C. and Plummer, L.N., 1985. PHREEQE – A computer program for geochemical calculations. *USGS Rep.* (USGS/WRI 80-96), U.S.A..

Posey-Dowty, J., Axtmann, E., Crerar, D., Borcsik, M., Ronk, A. and Woods, W., 1987. Dissolution rate of uraninite and uranium roll-front ores. *Econ. Geol.* 82, 184-194.

Read, D., Broyd, T.W. and Come, B., 1990. The CHEMVAL Project – An international study aimed at the verification and validation of equilibrium speciation and chemical transport models. *Proc. GEOVAL-90 Conf.*, Stockholm, Sweden.

Schlechter, R.S., Bryant, S.L. and Lake, L.W., 1987. Isotherm free chromotography: Propagation of precipitation/dissolution waves. *Chem. Eng. Comm.*, 58, 352-376.

Singer, P.C. and Stumm, W., 1970. Acid mine drainage – the rate limiting step, *Science*, 167, 1121-1123.

Walsh, M.P., Bryant, S.L., Schechter, R.S., and Lake, L.W., 1984. Precipitation and dissolution of solids attending flow through porous media. *Amer. Inst. Chem. Eng. J.*, 30, 317-327.

Wiersma, C.L. and Rimstidt, J.D., 1984. Rates of reaction of pyrite and marcasite with ferric iron at pH 2, *Geochim. Cosmochim. Acta*, 48, 85-92.

Appendix 1

The quasi-stationary state model.

Appendix 1

The quasi-stationary state model

Peter Lichtner

1. Introduction

The calculations are based on the quasi-stationary state approximation. In this approximation the time evolution of a geochemical system in response to mass transport is represented by a sequence of stationary states. Each stationary state represents the fluid composition corresponding to a different state of alteration of the host rock. The mathematical details can be found in Lichtner (1988). The work presented here is restricted to consideration of only the first stationary state. Calculations are carried out for pure advective transport in a single spatial dimension using a Lagrangian representation of the mass transport equations.

2. The pseudo-kinetic rate expression

Kinetic rate laws and associated rate constants for dissolution and precipitation reactions are known for very few minerals. Even for these minerals, however, considerable uncertainty exists in predicting the actual rate of reaction. This is because of difficulties in estimating the reacting surface area and the possible existence of boundary layer effects surrounding mineral grains (Murphy *et al.*, 1989). There is no certain algorithm for predicting the change in surface area with reaction progress. It may either increase as a result of etch pit formation, or decrease as the mineral grain completely dissolves. Since the reaction rate is proportional to the surface area, this leads to substantial uncertainty in predicting the rate of reaction. Finally for many minerals the actual reaction mechanism is unknown, such as for pyrite and uraninite, two examples of importance here. The question arises as to how accurately the kinetic rate law must be known to sensibly model mineral alteration processes.

For many geochemical systems, conditions of local equilibrium are not fulfilled and a kinetic description is necessary. For minerals for which the kinetic rate law is poorly known, one approach is to consider a pseudo-kinetic rate expression which incorporates

the basic requirement that the reaction rate tend towards zero as equilibrium is approached. For the overall mineral reaction

$$\sum_j \nu_{jm} A_j \rightleftharpoons \mathcal{M}_m \tag{1}$$

with solute species A_j, mineral M_m and stoichiometric reaction matrix ν_{jm}, equilibrium is defined by vanishing of the chemical affinity A_m defined by

$$A_m = -RT \ln K_m Q_m \tag{2}$$

where K_m denotes the corresponding equilibrium constant, R denotes the gas constant, T denotes the absolute temperature and Q_m denotes the ion activity product defined by

$$Q_m = \prod_j (\gamma_j m_j)^{\nu_{jm}} \tag{3}$$

with molality m_j and activity coefficient γ_j corresponding to the jth species. One simple form for the rate I_m of reaction (1) which satisfies the condition that the rate vanish at equilibrium is the expression:

$$I_m = -\kappa_m \left(1 - e^{-A_m/RT}\right) \tag{4}$$

where κ_m is a constant designating the pseudo-kinetic rate coefficient. The general form of the pseudo-kinetic rate has its foundations in transition state theory (*eg.* Aagaard and Helgeson, 1982). The rate I_m is positive for precipitation and negative for dissolution, with units of moles per unit volume per unit time. The mineral reaction rate represents an average over mineral surfaces contained in a representative elemental volume (REV) of the porous medium enclosing many mineral grains. It can be easily generalised to include a pH-dependence by multiplying by the activity of the hydrogen ion raised to a power, for example, or other factors that may be deemed important. The factor in brackets containing the affinity could also be replaced by any non-negative function of the affinity which vanishes at equilibrium. For surface-controlled mineral reactions, the rate coefficient κ_m can be interpreted as the product of the intrinsic rate constant κ_m times the specific surface area s_m:

$$\kappa_m = k_m s_m \tag{5}$$

The surface area is a function of reaction progress. One possible form of the surface area applicable to dissolution is given by the relation

$$s_m = s_m^0 \left(\frac{\phi_m}{\phi_m^0} \right)^{2/3} \tag{6}$$

where s_m^0 and ϕ_m^0 denote the initial surface area and mineral volume fraction. To apply this equation to precipitation it is necessary to make some assumption about the initial surface area and volume fraction. One possibility is to assume a fixed number of nucleation sites which do not change with reaction progress (Lasaga, 1984). Then, at the onset of precipitation, the initial surface area and volume fraction are equal to

$$s_m^0 = 2\pi r_m^2 \mathcal{N}_m \tag{7}$$

and

$$\phi_m^0 = \frac{4\pi}{3} r_m^3 \mathcal{N}_m \tag{8}$$

where spherical nuclei are assumed with radii r_m and number density N_m corresponding to the mth mineral. The expression for the surface area then becomes

$$s_m = \left[\frac{9\pi}{2} \mathcal{N}_m \right]^{1/3} \phi_m^{2/3} \tag{9}$$

For mixed surface- and transport-controlled reaction, the functional relation between κ_m and the intrinsic rate constant and mineral surface area can be much more complicated, involving such quantities as grain geometry, boundary layer thickness, solute diffusion coefficients and fluid flow velocity.

The pseudo-kinetic rate expression includes local equilibrium as a special case, while allowing deviations from equilibrium to be investigated. Close to equilibrium ($|A_m| \ll RT$) the rate is proportional to the chemical affinity according to the relation

$$I_m = -\frac{\kappa_m}{RT} A_m, \quad (|A_m| \ll RT) \tag{10}$$

Far from equilibrium $|A_m| \gg RT$, the pseudo-kinetic reaction rate I_m takes on two distinct limiting cases corresponding to precipitation and dissolution

$$I_m \sim \begin{cases} \kappa_m e^{|A_m|/RT} & > 0 \quad (-A_m \gg RT, \text{ precipitation}) \\ -\kappa_m & < 0 \quad (A_m \gg RT, \text{ dissolution}) \end{cases} \tag{11}$$

Therefore, far from equilibrium the reaction rate is constant for dissolution, but for precipitation grows exponentially with increasing disequilibrium.

While it might appear that an arbitrary reaction rate can be calculated merely by taking different values for the rate coefficient, this is not in fact the case. In principle, at least, as the rate coefficient is increased the reaction rate must approach the local equilibrium limit to within any desired degree of accuracy. This results in an upper bound on the rate coefficient. Larger values do not significantly alter the reaction rate from the local equilibrium limit. Kinetic effects only become important if the rate coefficient is smaller than this upper bound. The existence of such an upper limiting value greatly reduces the arbitrariness in the pseudo-kinetic rate expression and allows deviations from local equilibrium to be investigated without *a priori* knowledge of the actual rate law.

3. The multiple reaction path model

To solve the time-space representation of the full mass conservation equations describing the transport of solute species and their interaction with minerals is a formidable task. Therefore a much simpler problem is considered: that of calculating the fluid composition of a single packet of fluid as it traverses the flow path. This approach is referred to as a reaction path model because the fluid composition of the packet traces out a curved path in composition space that is parameterised by the travel time of the packet. The travel time is defined as the time it takes the packet of fluid to reach any particular point along the flow path. Distance along the flow path and travel time are related by the fluid velocity. In a multi-dimensional problem the packet is presumed to move along streamlines. Because transport by diffusion and dispersion is not included in the description, neighbouring streamlines do not interact with one another.

In a system involving mass transport, quantities of interest include the solute concentration and mineral modal abundance as a function of time at a fixed point in space. To obtain the spatial distribution and variation with time of minerals and solute concentrations in the reaction path model, it is necessary to consider many different

paths reflecting the changing composition of the host-rock. The fluid composition described by a single reaction path represents a stationary state, that is it has a fixed value at a given distance from the inlet. The time corresponding to a stationary state is determined by the particular state of alteration of the host-rock. Thus the time evolution of a geochemical system is obtained by considering a sequence of reaction paths representing a multiple reaction path model. Each path refers to a different state of alteration of the host-rock determined from the previous path. The equations determining a reaction path follow from the quasi-stationary state approximation to time-dependent partial differential equations describing the full transport problem. Because changes in the host-rock proceed on a much slower timescale than that required for the fluid composition to establish a stationary state, formation of a stationary state may be considered instantaneous. The very first reaction path describes the initial formation of the various mineral alteration zones. Subsequent paths describe their movement in time.

3.1. Mathematical formulation

A reaction path may be calculated for either an open or closed system. The latter corresponds, for example, to a batch reactor in which some chosen set of minerals is initially placed. A system involving fluid flow represents an open system with respect to the reacting minerals. The difference between an open and closed system can have important consequences for the reaction path of the fluid. In the batch reactor, product minerals are able to back-react until they either completely dissolve or come to equilibrium. For an open system product minerals are deposited along the flow path and are effectively removed from the system the instant they form. If, however, only a very small amount of any one product mineral is precipitated in the batch reactor, the time required for the product minerals to re-dissolve is small and in such cases the closed and open system reaction paths can be very similar.

For pure advective transport a reaction path is determined by specifying the starting composition of the fluid packet and the composition of the host-rock along the flow path. In what follows, homogeneous equilibrium is maintained within the aqueous phase. The path followed by the packet parameterised by the travel time t' is obtained by solving mass conservation equations given by the following set of ordinary differential equations

$$\frac{d\Psi_j}{dt'} = -\frac{1}{\phi}\sum_m \nu_{jm}\,\zeta_m\,I_m \qquad (12)$$

describing transport in a homogeneous porous medium with porosity ϕ. In this equation the quantity ψ_j denotes the generalised concentration of the jth primary species defined by

$$\Psi_j = \rho\left(m_j + \sum_i \nu_{ji}^{cx} m_i^{cx}\right) \tag{13}$$

where the superscript cx refers to aqueous complexes with molality m_i^{cx}, ν_{ji}^{cx} refers to the stoichiometric reaction matrix for the ith complex and ρ denotes the density of the aqueous solution. The factor ζ_m multiplying the reaction rate accounts for the appearance and disappearance of minerals along the flow path. Explicitly ζ_m is defined by

$$\zeta_m = \begin{cases} 1 & \text{if } \phi_m > 0 \text{ or } \phi_m = 0 \text{ and } A_m \leq A_m^0 \leq 0 \\ 0 & \text{if } \phi_m = 0 \text{ and } A_m > 0 \end{cases} \tag{14}$$

Here A_m^0 represents the threshold affinity below which nucleation commences. Thus ζ_m is unity for the cases where the mth mineral is present and is either dissolving or precipitating, or when it is not present but begins to precipitate; and is zero if the mineral is not present and the fluid composition is undersaturated with respect to the mineral.

A solution to the reaction path equation, Eqn.(12), defines a stationary state. It is solved subject to the initial condition

$$\Psi_j(0) = \Psi_j^0 \tag{15}$$

where Ψ_j^0 is defined by the initial fluid composition of the packet. Both the solute concentrations and mineral reaction rates are determined as a function of travel time of the packet. Thus these quantities depend on the distance travelled by a fluid packet from its starting point, but do not involve time explicitly. Time enters the transport equations implicitly as a parameter through the mineral modal abundances. The travel time is related to distance x along the flow path by the equation

$$t' = \frac{\phi x}{u} \tag{16}$$

for constant Darcy velocity u and porosity ϕ. For the case of constant porosity and Darcy flow velocity, the porosity enters the transport equations as a scale factor affecting the travel time of the packet but not the spatial dependence of mineral alteration zones and concentration profiles. These quantities are then independent of the porosity, all other quantities remaining the same. Reducing the porosity by a factor of two implies that the packet of fluid is in contact with twice the mineral surface area and therefore the reaction rate is twice as fast. Because the packet moves twice as fast, the identical spatial representation is obtained (Lichtner *et al.*, 1987).

An overall scale factor can be applied to the rate constants without altering the reaction path in composition space. The travel time must be scaled by the reciprocal factor. Under this transformation the differential equations describing the reaction path remain the same. Thus the reaction path depends only on the relative values of the rate constants, but not on their absolute magnitudes. The absolute magnitudes of the rate constants serve to fix the timescale for the evolution of the system.

Once a stationary state has been established, corresponding to a given state of alteration of the host rock, the change in mineral concentration at a fixed point is determined from the mineral mass transfer equations given by

$$\frac{\partial \phi_m}{\partial t} = \bar{V}_m I_m \tag{17}$$

where ϕ_m denotes the volume fraction and $\bar{V}_m$ the molar volume of the mth mineral. Integrating this equation over a time interval Δt at a fixed position x along the flow path yields

$$\phi_m(x, t + \Delta t) = \phi_m(x, t) + \Delta t \, \bar{V}_m I_m(x, t) \tag{18}$$

This expression gives the volume fraction of the mth mineral at time $t + \Delta t$ in terms of its value at time t and its rate of reaction I_m obtained from the stationary state at time t. With this newly obtained distribution of minerals, a new stationary state can be calculated and so on. The quasi-stationary state approximation assumes that the transient period during which the fluid composition establishes a stationary state can be completely neglected.

3.2. Numerical algorithm: MPATH

The stationary state transport equations must in general be solved numerically. Furthermore these equations present special difficulties because of their mathematical stiffness, resulting from the wide range of reaction rate constants often spanning many orders of magnitude. In the routine MPATH the stationary state solute transport equations are solved numerically using an implicit finite difference algorithm. Activity coefficient corrections are calculated using an extended Debye-Huckel algorithm. Redox reactions are incorporated in MPATH in terms of actual species in solution, rather than in terms of a hypothetical electron species. This guarantees conservation of electrons in the overall oxidation-reduction reaction. The code itself chooses the appropriate redox couple, which may change along the flow path according to solution concentrations and redox state.

Because of the drastic changes in concentration which may occur as a result of oxidation-reduction reactions, it is crucial to employ a basis switching algorithm so that only dominant species are used as primary species throughout the calculation. In addition an efficient adaptive step size algorithm is essential, allowing the time step to increase or decrease as smooth or rapid changes in concentration are encountered. Thus, for example, as the fluid packet crosses a redox front and the oxygen fugacity plummets towards zero, some species other than $O_{2(aq)}$ is chosen to represent the oxidation state of the fluid. Before the fluid packet reaches the redox front large time steps can be taken, but as the redox front is crossed extremely short time steps are required because of the rapidly changing concentrations of redox sensitive species across the front.

4. References

Aagaard, P., and Helgeson, H.C., 1982. Thermodynamic and kinetic constraints on reaction rates among minerals and aqueous solutions. I. Theoretical considerations, *Amer. J. Sci.* 282, 237-285.

Lasaga, A.C., 1984. Chemical kinetics of water-rock interactions, *J. Geophys. Res.* 89, 4009-4025.

Lichtner, P.C., Helgeson, H.C., and Murphy, W.M., 1987. Lagrangian and Eulerian representations of metasomatic alteration of minerals. In: H.C. Helgeson (Editor), Proc. NATO Advanced Study Institute on Chemical Transport in Metasomatic Processes, *Reidel, Dordrecht*, Holland, 519-545.

Lichtner, P.C., 1988. The quasi-stationary state approximation to coupled mass transport and fluid-rock interaction in a porous medium, *Geochim. Cosmochim. Acta*, 52, 143-165.

Murphy, W.M., Oelkers, E.H., and Lichtner, P.C., 1989. Surface reaction versus diffusion control of mineral dissolution and growth rates in geochemical processes, *Chem. Geol.* 78, 357-380.

List of SKB reports

Annual Reports

1977-78
TR 121
KBS Technical Reports 1 – 120
Summaries
Stockholm, May 1979

1979
TR 79-28
The KBS Annual Report 1979
KBS Technical Reports 79-01 – 79-27
Summaries
Stockholm, March 1980

1980
TR 80-26
The KBS Annual Report 1980
KBS Technical Reports 80-01 – 80-25
Summaries
Stockholm, March 1981

1981
TR 81-17
The KBS Annual Report 1981
KBS Technical Reports 81-01 – 81-16
Summaries
Stockholm, April 1982

1982
TR 82-28
The KBS Annual Report 1982
KBS Technical Reports 82-01 – 82-27
Summaries
Stockholm, July 1983

1983
TR 83-77
The KBS Annual Report 1983
KBS Technical Reports 83-01 – 83-76
Summaries
Stockholm, June 1984

1984
TR 85-01
Annual Research and Development Report 1984
Including Summaries of Technical Reports Issued during 1984. (Technical Reports 84-01 – 84-19)
Stockholm, June 1985

1985
TR 85-20
Annual Research and Development Report 1985
Including Summaries of Technical Reports Issued during 1985. (Technical Reports 85-01 – 85-19)
Stockholm, May 1986

1986
TR 86-31
SKB Annual Report 1986
Including Summaries of Technical Reports Issued during 1986
Stockholm, May 1987

1987
TR 87-33
SKB Annual Report 1987
Including Summaries of Technical Reports Issued during 1987
Stockholm, May 1988

1988
TR 88-32
SKB Annual Report 1988
Including Summaries of Technical Reports Issued during 1988
Stockholm, May 1989

1989
TR 89-40
SKB Annual Report 1989
Including Summaries of Technical Reports Issued during 1989
Stockholm, May 1990

Technical Reports

List of SKB Technical Reports 1990

TR 90-01
FARF31 –
A far field radionuclide migration code for use with the PROPER package
Sven Norman[1], Nils Kjellbert[2]
[1]Starprog AB
[2]SKB AB
January 1990

TR 90-02
Source terms, isolation and radiological consequences of carbon-14 waste in the Swedish SFR repository
Rolf Hesböl, Ignasi Puigdomenech, Sverker Evans
Studsvik Nuclear
January 1990

TR 90-03
Uncertainties in repository performance from spatial variability of hydraulic conductivities –
Statistical estimation and stochastic simulation using PROPER
Lars Lovius[1], Sven Norman[1], Nils Kjellbert[2]
[1]Starprog AB
[2]SKB AB
February 1990

TR 90-04
Examination of the surface deposit on an irradiated PWR fuel specimen subjected to corrosion in deionized water
R. S. Forsyth, U-B. Eklund, O. Mattsson, D. Schrire
Studsvik Nuclear
March 1990

TR 90-05
Potential effects of bacteria on radionuclide transport from a Swedish high level nuclear waste repository
Karsten Pedersen
University of Gothenburg, Department of General and Marine Microbiology, Gothenburg
January 1990

TR 90-06
Transport of actinides and Tc through a bentonite backfill containing small quantities of iron, copper or minerals in inert atmosphere
Yngve Albinsson, Birgit Sätmark,
Ingemar Engkvist, W. Johansson
Department of Nuclear Chemistry,
Chalmers University of Technology, Gothenburg
April 1990

TR 90-07
Examination of reaction products on the surface of UO_2 fuel exposed to reactor coolant water during power operation
R. S. Forsyth, T. J. Jonsson, O. Mattsson
Studsvik Nuclear
March 1990

TR 90-08
Radiolytically induced oxidative dissolution of spent nuclear fuel
Lars Werme[1], Patrik Sellin[1], Roy Forsyth[2]
[1]Swedish Nuclear Fuel and waste Management Co (SKB)
[2]Studsvik Nuclear
May 1990

TR 90-09
Individual radiation doses from unit releases of long lived radionuclides
Ulla Bergström, Sture Nordlinder
Studsvik Nuclear
April 1990

TR 90-10
Outline of regional geology, mineralogy and geochemistry, Poços de Caldas, Minas Gerais, Brazil
H. D. Schorscher[1], M. E. Shea[2]
[1]University of Sao Paulo
[2]Battelle, Chicago
December 1990

TR 90-11
Mineralogy, petrology and geochemistry of the Poços de Caldas analogue study sites, Minas Gerais, Brazil
I: Osamu Utsumi uranium mine
N. Waber[1], H. D. Schorscher[2], A. B. MacKenzie[3], T. Peters[1]
[1]University of Bern
[2]University of Sao Paulo
[3]Scottish Universities Research & Reactor Centre (SURRC), Glasgow
December 1990

TR 90-12
Mineralogy, petrology and geochemistry of the Poços de Caldas analogue study sites, Minas Gerais, Brazil
II: Morro do Ferro
N. Waber
University of Bern
December 1990

TR 90-13
Isotopic geochemical characterisation of selected nepheline syenites and phonolites from the Poços de Caldas alkaline complex, Minas Gerais, Brazil
M. E. Shea
Battelle, Chicago
December 1990

TR 90-14
Geomorphological and hydrogeological features of the Poços de Caldas caldera, and the Osamu Utsumi mine and Morro do Ferro analogue study sites, Brazil
D. C. Holmes[1], A. E. Pitty[2], R. Noy[1]
[1]British Geological Survey, Keyworth
[2]INTERRA/ECL, Leicestershire, UK
December 1990

TR 90-15
Chemical and isotopic composition of groundwaters and their seasonal variability at the Osamu Utsumi and Morro do Ferro analogue study sites, Poços de Caldas, Brazil
D. K. Nordstrom[1], J. A. T. Smellie[2], M. Wolf[3]
[1]US Geological Survey, Menlo Park
[2]Conterra AB, Uppsala
[3]Gesellschaft für Strahlen- und Umweltforschung (GSF), Munich
December 1990

TR 90-16

Natural radionuclide and stable element studies of rock samples from the Osamu Utsumi mine and Morro do Ferro analogue study sites, Poços de Caldas, Brazil

A. B. MacKenzie[1], P. Linsalata[2], N. Miekeley[3], J. K. Osmond[4], D. B. Curtis[5]
[1]Scottish Universities Research & Reactor Centre (SURRC), Glasgow
[2]New York Medical Centre
[3]Catholic University of Rio de Janeiro (PUC)
[4]Florida State University
[5]Los Alamos National Laboratory
December 1990

TR 90-17

Natural series nuclide and rare earth element geochemistry of waters from the Osamu Utsumi mine and Morro do Ferro analogue study sites, Poços de Caldas, Brazil

N. Miekeley[1], O. Coutinho de Jesus[1], C-L Porto da Silveira[1], P. Linsalata[2], J. N. Andrews[3], J. K. Osmond[4]
[1]Catholic University of Rio de Janeiro (PUC)
[2]New York Medical Centre
[3]University of Bath
[4]Florida State University
December 1990

TR 90-18

Chemical and physical characterisation of suspended particles and colloids in waters from the Osamu Utsumi mine and Morro do Ferro analogue study sites, Poços de Caldas, Brazil

N. Miekeley[1], O. Coutinho de Jesus[1], C-L Porto da Silveira[1], C. Degueldre[2]
[1]Catholic University of Rio de Janeiro (PUC)
[2]PSI, Villingen, Switzerland
December 1990

TR 90-19

Microbiological analysis at the Osamu Utsumi mine and Morro do Ferro analogue study sites, Poços de Caldas, Brazil

J. West[1], A. Vialta[2], I. G. McKinley[3]
[1]British Geological Survey, Keyworth
[2]Uranio do Brasil, Poços de Caldas
[3]NAGRA, Baden, Switzerland
December 1990

TR 90-20

Testing of geochemical models in the Poços de Caldas analogue study

J. Bruno[1], J. E. Cross[2], J. Eikenberg[3], I. G. McKinley[4], D. Read[5], A. Sandino[1], P. Sellin[6]
[1]Royal Institute of Technology (KTH), Stockholm
[2]AERE, Harwell, UK
[3]PSI, Villingen, Switzerland
[4]NAGRA, Baden, Switzerland
[5]Atkins, ES, Epsom, UK
[6]Swedish Nuclear and Waste Management Co (SKB), Stockholm
December 1990